

Integration of regional gravity modeling, subsidence analysis, and source rock maturity data to understand the tectonic and hydrocarbon evolution of the Permian Basin, West Texas

Hualing Zhang¹, Paul Mann¹, Dale E. Bird², and Kurt Rudolph³

Abstract

The Permian Basin of West Texas and southeast New Mexico is currently the most prolific oil-producing basin in the United States. This region experienced deformation and extreme rates of subsidence (up to 500 m/my), especially during the Late Paleozoic. To investigate the larger scale crustal geometry of the Permian Basin, its tectonic evolution, and the distribution of its most productive late Paleozoic source rocks, we have created regional 2D and 3D gravity models that incorporate density and lithologic controls from wireline logs, published seismic refractions, and regional cross sections. These gravity models better define a regional north-east-trending gravity low called the Abilene gravity minimum (AGM) that underlies the northern Permian Basin. We infer this feature to be underlain by a low-density assemblage of Precambrian granitic and metasedimentary rocks. Structural inversion from the gravity model shows that the top of the lower crust and the Moho is presently depressed beneath the AGM. Subsidence analysis defines five tectonic phases from Cambrian to recent with maximum subsidence during the main, late Paleozoic deformational phase resulting in deposition of sediments up to 2.4 km thick. We have determined that the geobody under the AGM acted as a zone of preferential weakness in a “broken foreland basin” setting that accommodated regional shortening related to the Marathon orogeny and to other coeval orogenies along the Sonoran margin and Nevadan margin. Our new regional map of the top basement defines the limits of deep basinal areas that may host the most productive and thermally mature, late Paleozoic source rock kitchens — some of which are localized in depocenters controlled in part by syncollisional, left-lateral strike-slip faults that align with the edges of the AGM. Our results show a deeper basement ranging from 5.5 to 6.2 km in the Delaware basin that predicts a broader zone of source rock thermal maturity.

Introduction

Geologic and tectonic setting

The Permian Basin of West Texas and southeast New Mexico is located in the distal foreland area of the Ouachita-Marathon-Sonoran fold-thrust belt (Yang and Dorobek, 1995; Poole et al., 2005; Ruppel, 2019) and was likely subjected to other, more distant, late Paleozoic orogenic effects from the southwestern and western margins of North America (Leary et al., 2017; Ewing, 2019). The Permian Basin covers an area of 220,000 km² of West Texas and southeastern New Mexico and includes three major components: in the west, the Delaware Basin (DB) contains up to 6.4 km, mainly Paleozoic strata that dip eastward; in the center is the relatively elevated

area of the north–south-trending Central Basin Platform (CBP); and in the east, the Midland Basin (MB) contains up to 4.4 km of mainly Paleozoic strata (Matchus and Jones, 1984; Dutton et al., 2005; Figure 1).

Previous interpretations of the tectonic controls on the Permian Basin subsidence

Previous regional geologic studies by Graham et al. (1975), Kluth and Coney (1981), Dickinson and Lawton (2003), and Poole et al. (2005) all characterized the Marathon-Ouachita orogeny as a diachronous, late Paleozoic collision that youngs from the south-central USA (late Mississippian) to West Texas and New Mexico (Permian) and into northern Mexico (Permian) along

¹University of Houston, Department of Earth and Atmospheric Sciences, Houston, Texas 77204–5007, USA. E-mail: hzhang67@uh.edu (corresponding author); pmann@uh.edu.

²University of Houston, Department of Earth and Atmospheric Sciences, Houston, Texas 77204–5007, USA and Bird Geophysical, Houston, Texas 77084, USA. E-mail: dale@birdgeo.com.

³University of Houston, Department of Earth and Atmospheric Sciences, Houston, Texas 77204–5007, USA and Rice University, Houston, Texas 77005, USA. E-mail: kwrudolph@comcast.net.

Manuscript received by the Editor 26 February 2020; revised manuscript received 7 October 2020; published ahead of production 30 October 2020; published online 20 January 2021. This paper appears in *Interpretation*, Vol. 9, No. 1 (February 2021); p. T161–T181, 18 FIGS.

<http://dx.doi.org/10.1190/INT-2020-0065.1>. © 2021 Society of Exploration Geophysicists and American Association of Petroleum Geologists

a suture zone between Gondwana and Laurentia. Orogenic deformation was proposed to have begun in the Late Mississippian near the Black Warrior Basin in western Alabama and northern Mississippi and migrated southwestward, creating a set of foredeep basins that include the Arkoma Basin of southeastern Oklahoma and Central Arkansas and the Fort Worth Basin of northern Texas as the result of the flexure of the continental margin of North America by a north- and northwest-directed thrust sheet (Graham et al., 1975; Dickinson and Lawton, 2003). Along the southern margin of the Permian Basin, thin-skinned convergence emplaced the allochthonous Marathon fold-thrust belt, whereas thick-skinned deformation formed the Devils River Uplift during Pennsylvanian and Wolfcampian time (Ewing, 2019).

Previous interpretations by Graham et al. (1975) and Kluth et al. (1981) proposed that the Ouachita-Marathon collisional orogeny was the main driver for thick-skinned deformation, which formed part of the Ancestral Rocky Mountain (ARM) system and invoked the ongoing collision of India with the Asian continent as a modern, structural analog. More recent interpretations of the Ouachita-Marathon belt and ARM to the north have emphasized that many of these late Paleozoic

basement uplifts trend north-south and therefore reflect shortening from either the northwest-trending Sonoran margin to the southwest in Mexico or the north-south-trending Nevadan margin in the western USA (Dickinson and Lawton, 2003; Poole et al., 2005; Leary et al., 2017; Ewing, 2019).

Contractional deformation and intricate faulting controlled the formation of the two late Paleozoic subbasins of the Permian Basin: the MB and DB — along with structural highs that include the CBP, the Diablo Platform, and the Ozona Arch (OA) (Hills, 1972; Frenzel et al., 1988; Ewing, 2019) (Figure 1). Detrital zircon studies indicate that sediment sources into the synorogenic Permian Basin included (1) the distal Appalachian orogenic belt far to the west or east (Soreghan and Soreghan, 2013; Gao et al., 2019; Xie et al., 2019), (2) the Ouachita orogenic belt in the southeast (Soreghan and Soreghan, 2013; Xie et al., 2019), and (3) peri-Gondwanan terranes from nearby southern orogenic highland in the southwest (Gao et al., 2019; Xie et al., 2019; Liu and Stockli, 2020; Soto-Kerans et al., 2020).

Hydrocarbon significance

The Permian Basin is the most prolific oil-producing basin in the United States, with an estimated 5 billion barrels of proven conventional oil reserves (Dutton et al., 2004, 2005). The Permian Basin has generated hydrocarbons for over a century and has supplied more than 33.4 billion barrels of oil and approximately 118 trillion cubic feet of natural gas as of September 2018 (EIA report, 2018).

With advances in technology such as hydraulic fracturing and horizontal drilling, unconventional oil and gas reservoirs have become an important target for petroleum exploration in the Permian Basin. Unfortunately, high-quality 2D and 3D seismic coverage has not been made widely available for research studies, including Ewing (2019) and this study. For this reason, we rely on public access potential field data (Daniels et al., 2002; Pavlis et al., 2012) to help us understand the regional tectonic controls on the basin, including its broader context in the late Paleozoic tectonic events that include deformation along the Ouachita-Marathon belt and within the coeval ARM orogeny.

Objectives of this study

The objective of our study is to better understand the structural and depositional responses of the Permian Basin region to the potentially combined effects of the Marathon-Ouachita orogeny and the ARM orogeny by integrating subsidence history, basin structure, and the underlying crustal structure of the Permian Basin. A prominent 650 km long, northeast-trending negative gravity anomaly exhibits an average magnitude of 136 mGal, extends across the northern Permian Basin, and forms one of the main topics of our regional study (Figure 1b).

This gravity anomaly was named the Abilene gravity minimum (AGM) by Adams and Keller (1994), who infer

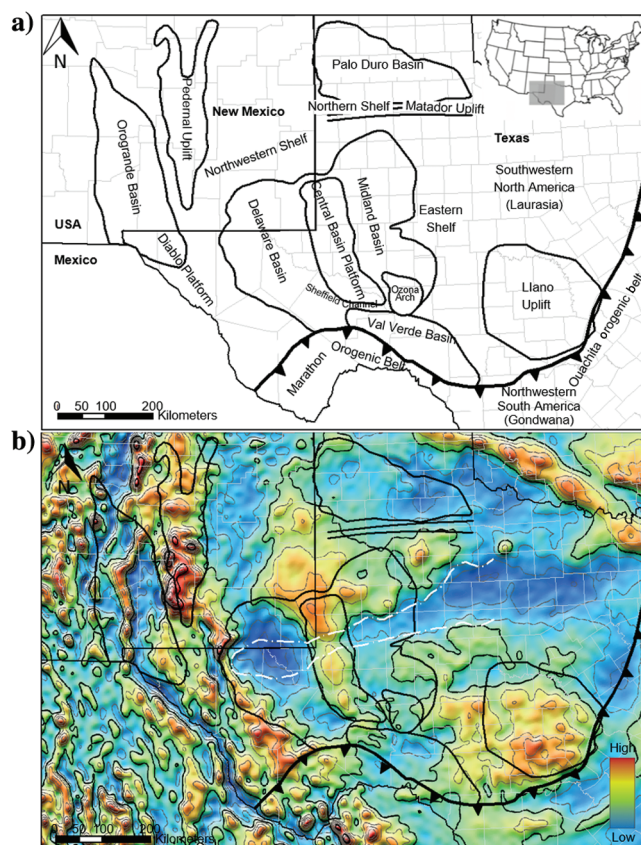


Figure 1. (a) Geographic setting of the Permian Basin region showing major basin names. (b) Vertical gradient of gravity anomalies of the Permian Basin region showing gravity expression of major basins and the AGM outlined by the white dashed line (modified from Garcia et al., 2014).

that it represented a highly elongated batholith of Early Mesoproterozoic age (Adams and Miller, 1995, 1996; Keller, 2019). Adams and Keller (1994, 1996) build regional 2D gravity models of the deep structure in the Permian Basin. In his most recent gravity models, Keller (2019) reinterpret the AGM as underlain by Early Mesoproterozoic granitic and metasedimentary rocks and/or sediments with lower density compared to the rest of the upper crust. A well penetrated the basement in the AGM southwest of Abilene and encountered granite with a U-Pb age of 1078 ± 23 Ma (Ewing et al., 2019).

Ewing et al. (2019) describe the diverse Proterozoic basement in the Permian Basin in terms of its lithologic compositions and radiometric ages. The Southern Granite-Rhyolite Province to the north of the AGM is characterized by interbedded volcanic and sedimentary rocks and sills (1400–1320 Ma) (Ewing et al., 2019). To the southwest of the AGM, the Permian Basin basement is considered to be correlative with the exposed Llano Uplift (Mosher, 1998).

The tectonic origin of the AGM is not well understood. Adams and Keller (1996) attribute the AGM to an elongated batholith formed by Precambrian subduction processes that were later modified by orogenic processes

along the suture between the southern edge of the Laurentian continent and accreted, island arc terranes to the south. Mosher (1998) propose that this region formed as a Precambrian back-arc basin that accompanied north-dipping subduction along the structural boundary, now known as the Llano Front.

To understand the origin and deformational history of the enigmatic AGM, our study incorporates 296 industry wells with seismic refraction station controls to generate 2D and 3D gravity models for understanding the crustal framework of the Permian Basin, including its relation to the AGM. Compared to previous gravity models, our study added the lower crust and mantle layers to provide a complete crustal structure of the region. The results of the deep structure were then compared to basin modeling results on the two most prolific Permian Basin source rocks (the Woodford and the Wolfcamp shales) to provide insights into future hydrocarbon exploration (Figure 2).

Data and methods

Well data

Well logs used for 2D and 3D gravity modeling include 166 wells provided by TGS and 130 wells provided

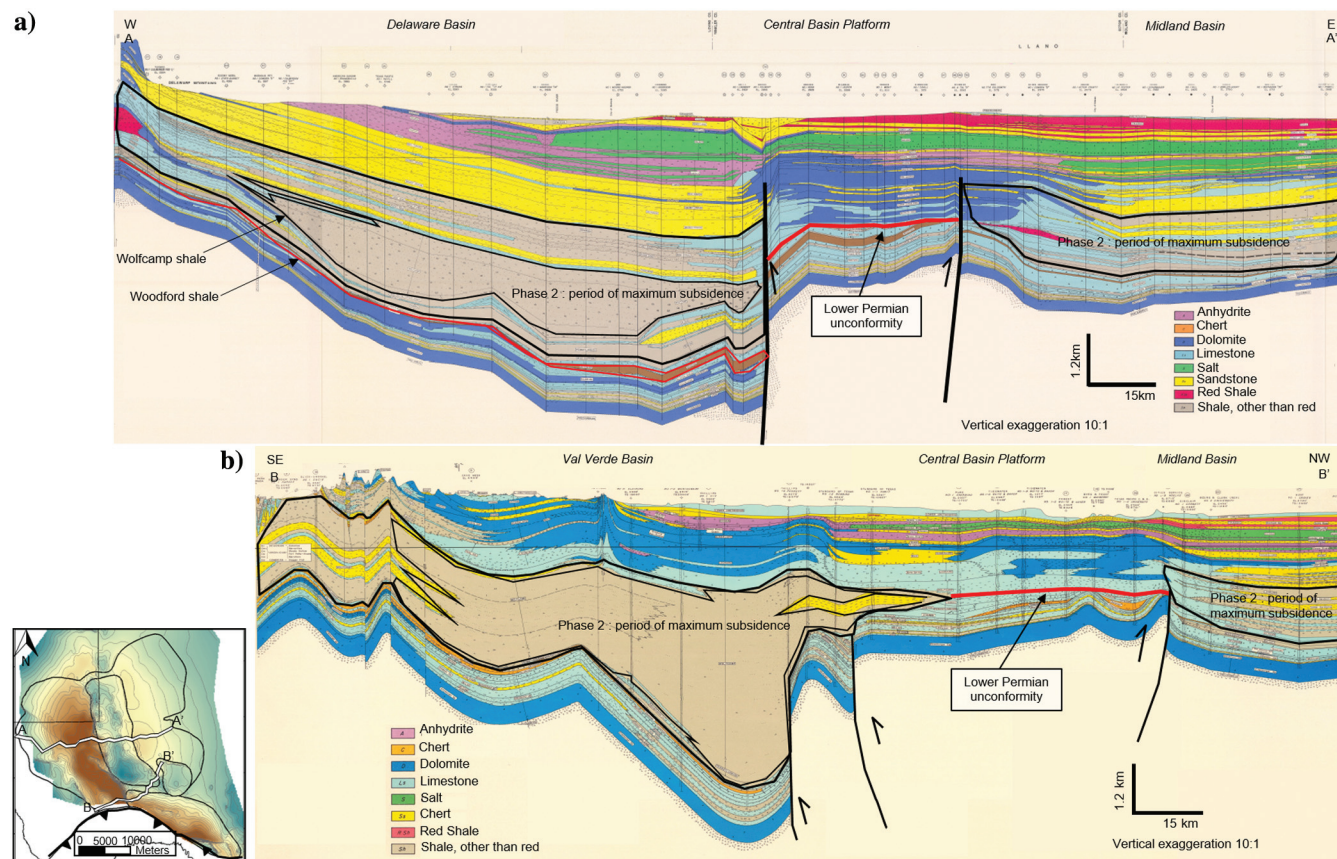


Figure 2. (a) Regional, east–west trending, 193 km long cross section across DB, CBP, and MB showing sediment packages thickening toward the high-angle normal faults bounding the CBP (modified from Matchus and Jones, 1984). Lower Permian unconformity was observed on the CBP. (b) Regional, southwest–northeast-trending, cross section across the VVB, CBP, and MB showing synorogenic, clastic wedge thickening toward the high-angle reverse faults bounding the CBP (modified from Feldman and Chairman, 1962). The lower Permian unconformity was observed on the CBP.

by Enverus (Figure 3). Most wells are deep enough to reach the Ordovician Ellenburger Formation, which lies within 100–500 m of the top of the crystalline basement. Using previous publications (Matchus and Jones, 1984) and 30 wells that contain formation tops provided by Enverus as control points, six key formation tops were correlated, which include the (1) top of the Rustler Formation, (2) top of the Leonardian (Cisuralian), (3) top of the Strawn Formation, (4) top of the Barnett Formation, (5) top of the Devonian (Woodford Formation), and (6) top of the Ellenburger Formation. The top of the Leonardian is defined as the top of the Bone Spring Formation in the DB, the top of the Spraberry Formation in the MB, and the top of the Glorieta Sandstone Member in the CBP.

In this study, we conducted basin modeling of six representative wells from the Permian Basin using PetroMod 1D (Figure 3). The basin models were used to better understand the uplift and subsidence history and its relationship to the Marathon-Ouachita orogeny and the ARM orogeny (Leary et al., 2017; Ewing, 2019). Well logs and cross sections for basin modeling were compiled from previous publications by Feldman and Chairman (1962) and Matchus and Jones (1984).

Gravity and magnetic data

Open-file gravity and magnetic data were used for developing integrated geophysical models to infer deep structure and basin depocenters. Gravity data over the study region combine onshore Bouguer gravity anomalies of the Decade of North American Geology (DNAG) grav-

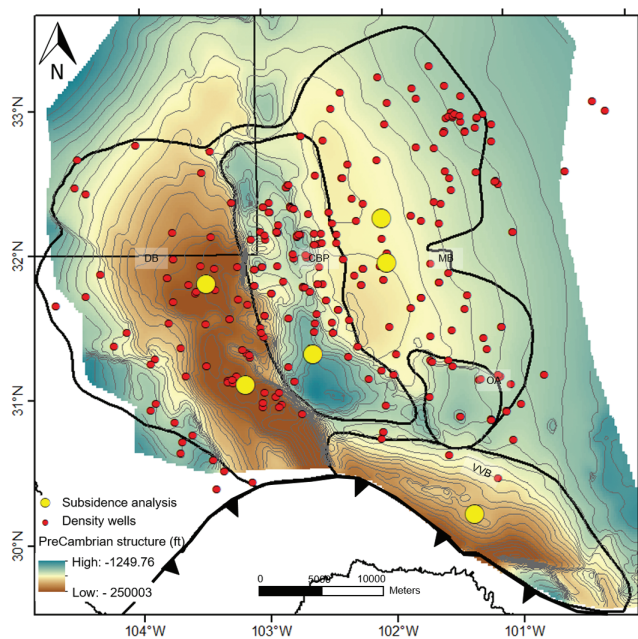


Figure 3. Structural map of the top of the Precambrian basement beneath the Permian Basin by Ruppel et al. (2008) showing the locations of well logs (the red dots) used in this study for well correlations and gravity modeling. The locations of the wells used for subsidence analysis are shown by the yellow dots.

ity grid that is spaced at 6 km and compiled by the National Oceanic and Atmospheric Administration. The DNAG grid covers the US, and the EGM2008 gravity model from Pavlis et al. (2012) covers Mexico (Figure 4a).

Residual Bouguer gravity anomalies were then derived by subtracting a 10 km upward continuation of Bouguer anomalies from the original Bouguer gravity grid (Figure 4b). The derived residual gravity anomalies enhance short wavelengths at the expense of long wavelengths, thus improving the imaging of geologic features with subtle gravity anomalies. Magnetic data over the study area are from magnetic anomaly maps of the North America grid that was compiled by the USGS (Daniels et al., 2002) (Figure 5).

2D gravity model

All gravity modeling was performed using Geosoft's Oasis montaj software. Three regional 2D gravity models were generated, incorporating density and structural controls of the six key formations from well-log interpretation, regional cross sections from Matchus and Jones (1984), refraction stations for regional control of basement and Moho horizon depths, and from previously published gravity models by Adams and Keller (1996).

The density inputs of the upper crust, lower crust, and upper mantle used in our model were 2.75, 2.9, 3.3 g/cm³, respectively. These density values were consistent with ranges of densities applied to the crust and mantle layers in numerous studies, including 2D and 3D models (Adams and Keller, 1996; Hall et al., 2018). The 2D gravity models were also compared with the 3D gravity inversion results to test the consistency of the crustal structural details.

3D gravity model

The 3D gravity model uses structural and density grids that incorporate inputs from well interpretations and previous publications. The basement grid was calculated by subtracting the Ellenburger isopach, as mapped by Ruppel et al. (2008) from the top of the Ellenburger horizon. Our initial input Moho grid was derived from an isostatic calculation (Blakely, 1995):

$$dm = h(\rho_t/\Delta\rho) + ds. \quad (1)$$

In this equation, all depths are in km, dm and ds are the Moho depth with the compensation depth (33 km) at the shoreline (the isobaric Moho depth), h is elevation, ρ_t is the average crustal density, and $\Delta\rho$ is the density contrast at the base of the crust. Our initial input for the top of the lower crust grid was created by splitting the depth from the basement to the Moho in half.

The density inputs of the upper crust, lower crust, and upper mantle used in our model were 2.75, 2.9, 3.3 g/cm³, respectively. Sedimentary rock densities were extracted from bulk density logs and gridded. Structural inversion of the Moho in our 3D gravity model was performed using a method of the Fourier transform

technique for calculating potential field anomalies produced by uneven layers described by Parker (1973).

Results from 2D gravity modeling

Density variations

Stratigraphy and lithology within the two subbasins and the CBP vary greatly (Figure 2), especially during the orogenic period from the Late Mississippian to the Mid Permian. For example, the Wolfcamp Formation in the MB contains a mixture of limestone, silt, and shale whereas the Wolfcamp Formation in the CBP is dominated by carbonate rocks (Figure 2). Therefore, by comparing the density values from bulk density logs and previous studies (Djeddi, 1979; Adams and Keller, 1996), we divided the sedimentary rocks above the basement into seven layers (Figure 6). Each density layer consists of one or more formations that share similar density values, and the density within these similar layers was considered constant. Density values vary from 2.45 to 2.8 g/cm³ as a result of lithologic variation between the formations (Figure 6).

Model A-A'

Model A-A' is a 292 km long, north-south regional cross section through the MB (Figure 7). This model was modified from a previous gravity model by Adams and Keller (1996) by adding the lower crust and the

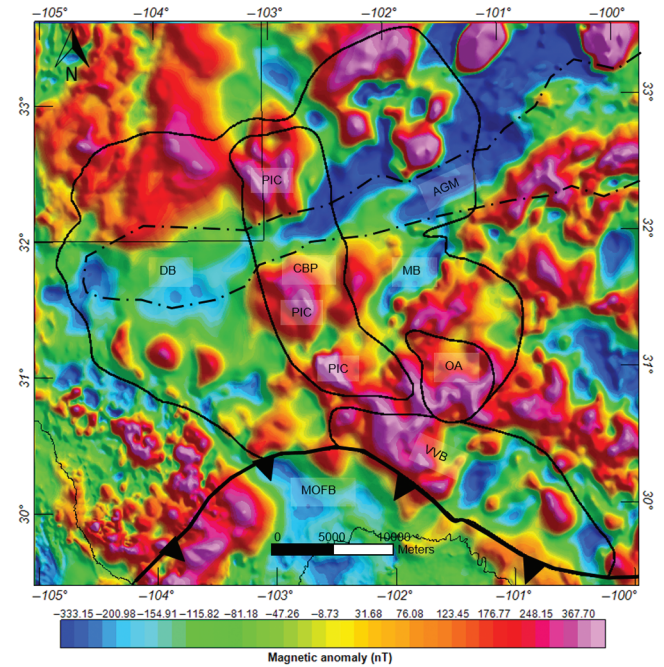


Figure 5. (a) Total magnetic field anomalies of the Permian Basin study area from the North America grid compiled by the USGS. The magnetic high anomalies in the Central Basin indicate potential areas of igneous intrusions, such as the PIC. The AGM forms a linear magnetic low across the northern Permian Basin.

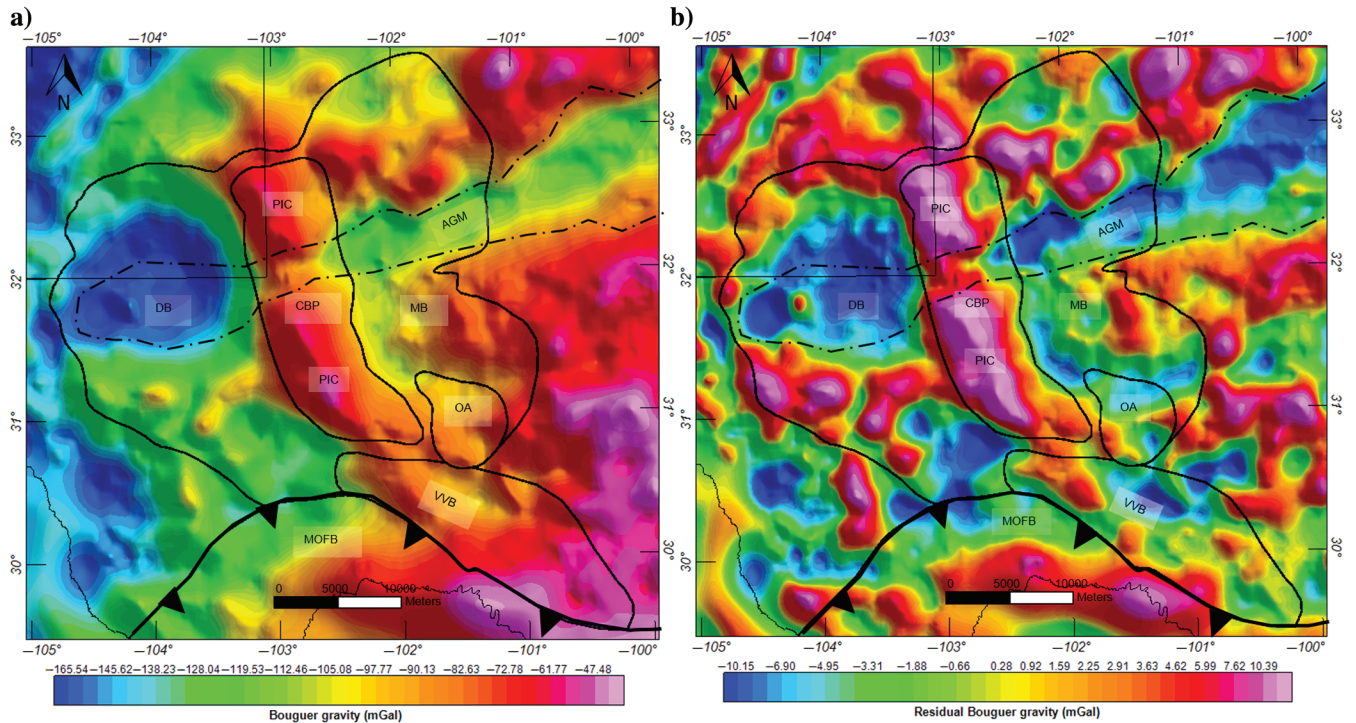


Figure 4. (a) Bouguer gravity anomalies of the Permian Basin region, which combines the DNAG gravity grid on the US side and the EGM2008 gravity grid on the Mexico side, showing major basins and structural high. The AGM is an east-northeast-trending major gravity low in the northern Permian Basin. The Pecos Intrusive Complex (PIC) shows as north-northwest-trending gravity high in the CBP. DB, Delaware Basin; MB, Midland Basin; CBP, Central Basin Platform; VVB, Val Verde Basin; OA, Ozona Arch; MOFB, Marathon-Ouachita orogenic fold belt; and PIC, Pecos Intrusive Complex. (b) Residual Bouguer gravity anomalies of the Permian Basin study area derived from the Bouguer gravity. The boundary of the AGM is identical on the residual Bouguer gravity anomaly map.

System	Delaware	g/cm ³	CBP	g/cm ³	Midland	g/cm ³	Litho.	Tectonic phases
Quaternary	Holocene Sand		Holocene Sand		Holocene Sand			5. Basin reactivation phase
Tertiary		2.45		2.45		2.45		4. Stable platform phase
Cretaceous								
Jurassic								
Triassic								
Permian	Rustler	2.57	Rustler	2.67	Rustler	2.54		3. Postdeformational, subsidence phase
	Cherry Canyon		San Andres		San Andres			2. Main deformational phase
	Bone Spring		Glorieta		Spraberry			
	Wolfcamp	2.59	Wolfcamp	2.68	Wolfcamp	2.54		
Penn.	Strawn	2.56	Strawn	2.60	Strawn	2.58		
Mississippian	Barnett	2.56	Barnett	2.58	Barnett	2.57		1. Precollisional, Tobasa Basin and transition phase
	Mississippian Limestone		Mississippian Limestone		Mississippian Limestone			
Devonian	Woodford		Woodford		Woodford			
Silurian	Fusselman	2.71	Fusselman	2.65	Fusselman	2.67		
Ordovician	Simpson		Simpson		Simpson			
	Ellenburger	2.8	Ellenburger	2.8	Ellenburger	2.8		

Dolomite	Limestone	Anhydrite	Chert
Sandstone	Siltstone	Shale	

Figure 6. Density intervals assigned for gravity modeling with simplified stratigraphy and generalized lithology of the Permian Basin region. Density values were extracted from density logs from wells shown as the red circles in Figure 3. The dashed lines indicate major unconformities. Density values change from 2.45 to 2.8 g/cm³ due to the lithologic variation between formations.

upper mantle layers as well as additional constraints from well logs and a published seismic refraction station (Gaherty, 2004). Model A-A' crosses the AGM in the northern MB and shows that the AGM was produced by a geobody of lower density (2.64 g/cm³) compared to the adjacent upper crust. Although the density of the AGM is similar to a granitic intrusion, the geobody underlying the AGM produces a magnetic low anomaly, which differs from a granitic body that generally produces magnetic high anomalies (Figure 5). Based on our observations, our modeling results, and previous interpretations by Keller (2019), we interpret the AGM as a mixture of granitic and metasedimentary rocks with a lower density relative to the upper crust.

Another elongate and subparallel gravity low in the southern MB produces gravity and magnetic anomalies similar to the AGM (Figures 5 and 7). This gravity low is related to a distinct source similar to the metasedimentary or granitic belt underlying the AGM. Model A-A' shows the presence of an intrusive mafic body in the northern MB (Figure 7), which was inferred from its distinctive magnetic amplitude (Adams and Keller, 1996; Keller, 2019; Figure 5). The model shows that the total crustal thickness of the MB ranges from 33 to 35 km.

Model B-B'

Model B-B' is a 240 km long, north-south regional cross section through the DB (Figure 8). This model is roughly coincident with the section shown by Adams

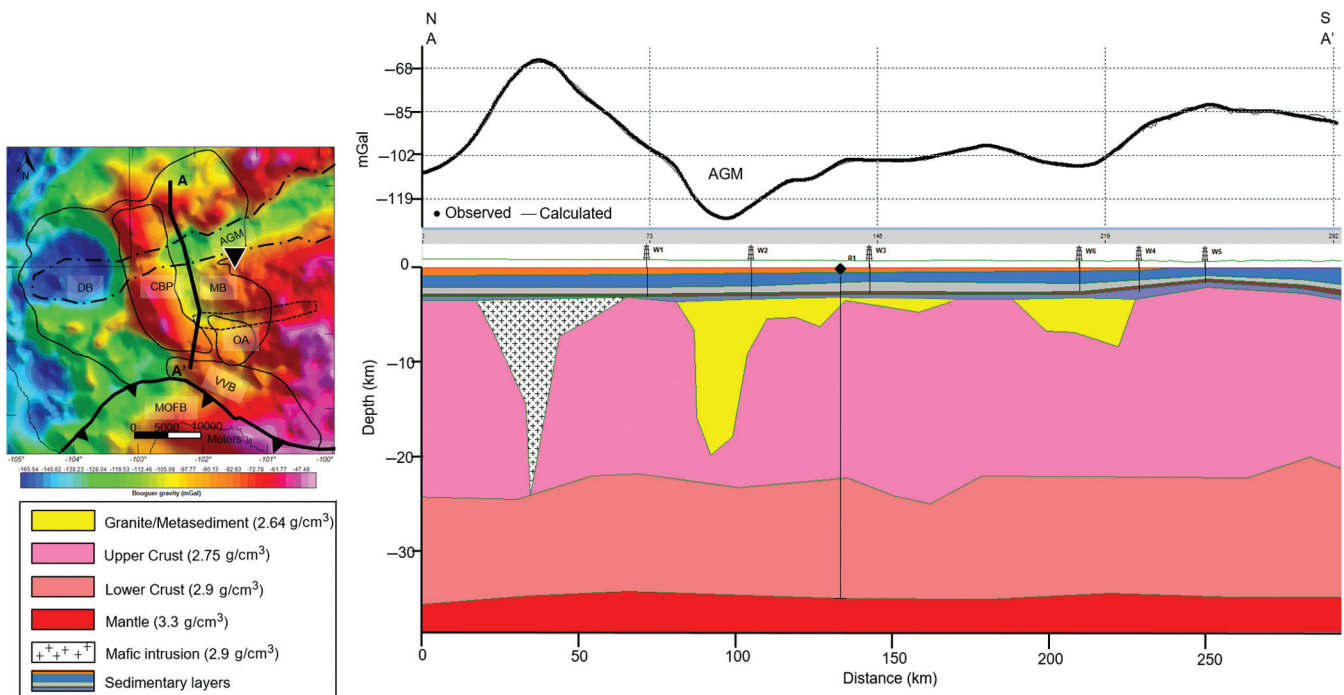


Figure 7. Regional 2D gravity modeling A-A' trending north-south across the MB and collinear with a previous gravity model by Adams and Keller (1996). The model location is shown in the base map to the left. The dotted line shows the location of an inferred and elongate mixture of granitic and metasedimentary rock 50 km to the south and subparallel to the AGM. A single refraction station is shown as an inverted black triangle on the base map that was projected onto the plane of the section to constrain the model along A-A'. The calculated gravity response closely fits the observed gravity signal.

and Keller (1996) (Figure 9). Our model B-B' contains more constraints from well logs and refraction stations (Romney et al., 1962; Jackson and Pakiser, 1966; Mitchell and Landisman, 1971; Dumas, 1982) than the previous model of Adams and Keller (1996).

We added the lower crust and the upper mantle layers to model B-B' to better constrain the deeper crustal structure. This model crosses the AGM in the northern DB. Like model A-A', the geobody that produced the gravity low in this area was interpreted as a mixture of granitic and metasedimentary rocks. The modeled geobody is much wider (127 km) compared to the MB (60 km), and its thickness ranges from 2.7 to 12.4 km.

The P-wave velocity from seismic refraction stations across the AGM showed a lower value of 5.95 km/s compared to other locations (averaging 6.7 km/s). This observation further supports the inferred presence of the mixture of granite and metasedimentary rocks underlying the AGM (Keller, 2019). The presence of an intrusive mafic body in the southern DB was inferred from its distinctive magnetic amplitude (Adams and Keller, 1996; Keller, 2019) (Figure 5). The total crustal thickness across this area is thicker than the MB, and it ranges from 36.9 to 38.8 km.

Model C-C'

Model C-C' was constructed along the east–west regional cross section from Matchus and Jones (1984). Model C-C' passes from west to east through the DB,

the CBP, and the MB (Figure 9). Model C-C' was also well constrained using well logs and refraction data (Dumas, 1982; Gaherty, 2004; Shen et al., 2013). Model C-C' is consistent with models A-A' and B-B' at their intersection points.

As shown in Figure 8, model C-C' traverses through the AGM in the DB and partially in the MB. The AGM in the eastern DB was interrupted by an intrusive mafic body whose location was constrained by its distinctive magnetic signal as an isolated magnetic high. The depth to Moho and depth to the top of the lower crust is shallower in the CBP as the likely result of less sedimentary overburden and the absence of the mixture of granitic and metasedimentary rocks in the upper crust as shown in Figure 8. The total crustal thickness is the least (31.9 km) along model C-C' beneath the CBP. Similar to the previous two models, the Moho on model C-C' is relatively deeper beneath the center of the AGM (average 42 km).

Results from 3D gravity modeling

Density variation

Based on the bulk density logs, the sediment density within the Permian Basin region varies vertically between formations and laterally within the same stratigraphic intervals. Similar to 2D gravity modeling, we divided the sedimentary layers into seven density layers separated by seven horizons.

The seven density layers include (1) surface stations (topography) — top Rustler Formation, (2) top Rustler

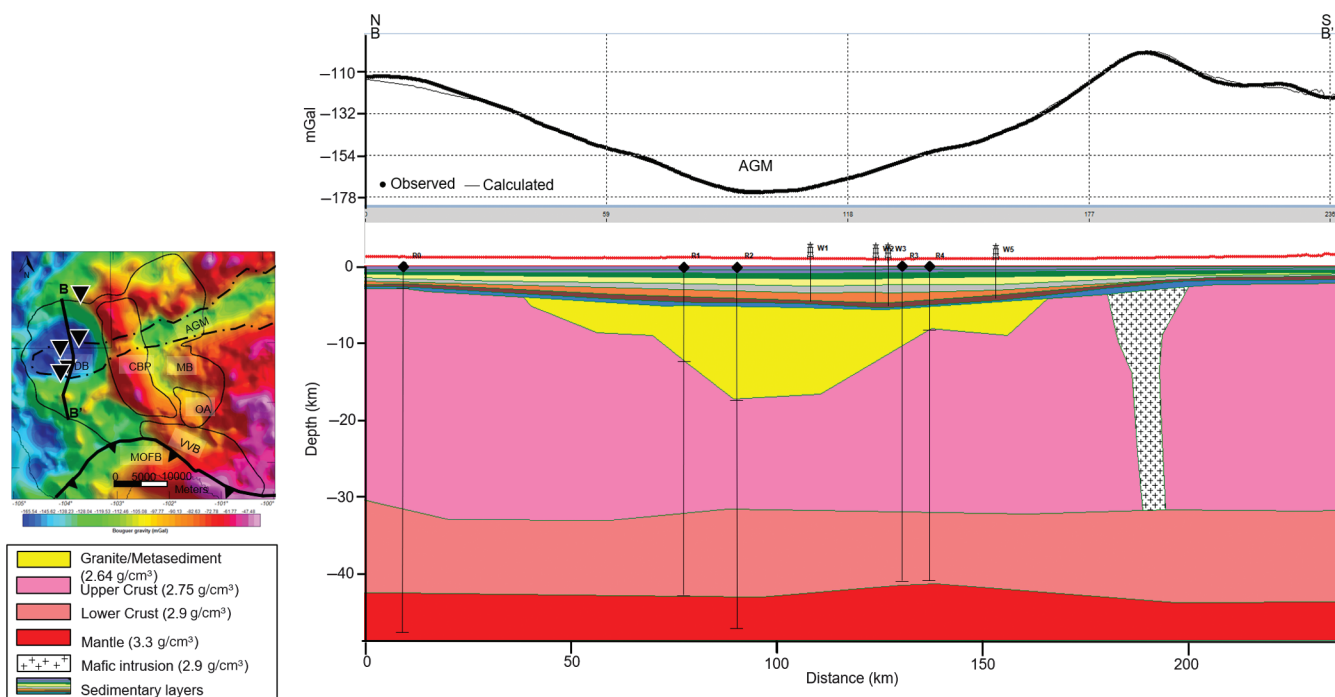


Figure 8. Regional 2D gravity model B-B' trending north–south across the DB and collinear with a previous gravity model by Adams and Keller (1996). The model location is shown on the base map on the left. Five refraction stations are shown as the inverted black triangles on the base map, and they were projected onto the plane of the section to constrain the model along B-B'. The calculated gravity response closely fits the observed gravity signal. A mafic intrusion body was added in the south based on the magnetic signal from Figure 5.

Formation — top of the Leonardian, (3) top of the Leonardian — top of the Strawn Formation, (4) top of the Strawn Formation — top of the Barnett Formation, (5) top of the Barnett Formation — top of the Devonian (Woodford Formation), (6) top of the Barnett Formation — top of the Ellenburger Formation, and (7) top of the Ellenburger Formation — top basement. Each of these horizons was interpreted and correlated across the study region. The top of the Leonardian is defined as the top of the Bone Spring Formation in the DB, the top of the Spraberry Formation in the MB, and the top of the Glorieta Sand Member in the CBP.

Average density values within each layer were calculated at every well location (1614 measurements) to incorporate density variations within the Permian Basin and were then gridded (Figure 10). The average density between the Ellenburger Formation and the basement varies from 2.66 to 2.85 g/cm³ (Figure 10a). Higher density was observed in the western DB and central MB. Areas with low-density anomalies may be due to the effect of karst weathering within the lower Ellenburger Formation (Loucks, 2008).

Density values vary greatly throughout the study region from the top Devonian to the top Strawn Formation because of lithologic differences (Figure 2) between the two subbasins and the platform (Figure 10b–10d). The CBP is more carbonate-dominated compared to the two subbasins, which are clastic-dominated. The DB consists of thicker, fine-grained sediments compared to those of the MB. Density values become more uniform between

the top of the Leonardian and the top Rustler and show a higher value on the platform and lower values within the two subbasins (Figure 10e). The average density above the Rustler Formation was set constant to 2.45 g/cm³ based on Adams and Keller (1996) because the density logs used in this study did not cover the interval above the Rustler Formation.

3D gravity modeling framework

Formation tops bounding the density intervals were correlated using 296 well logs as the structural input for the 3D gravity model (Figure 11). In general, the DB received thicker sediments, as shown by the deeper depocenters shown in Figure 11a–11d. The top Ellenburger Formation reaches a depth of 6200 m below sea level beneath the deepest area of the central DB (Figure 11a).

The CBP is a structural high separating the DB and MB. During the upper Demioesian (upper Strawn) through lower Wolfcamp time, the CBP underwent up to 1000 m of uplift and erosion to create a hiatus known as the Lower Permian unconformity (Matchus and Jones, 1984; Figure 10d). The Lower Permian (Wolfcampian and Leonardian) section is relatively uniform in thickness in the DB and MB (Figure 11e), and it was partially filled by the top of the Rustler Formation (Figure 11f).

The 3D gravity model includes 10 layers, including the same seven sedimentary layers described above, the upper crust, the lower crust, and the upper mantle.

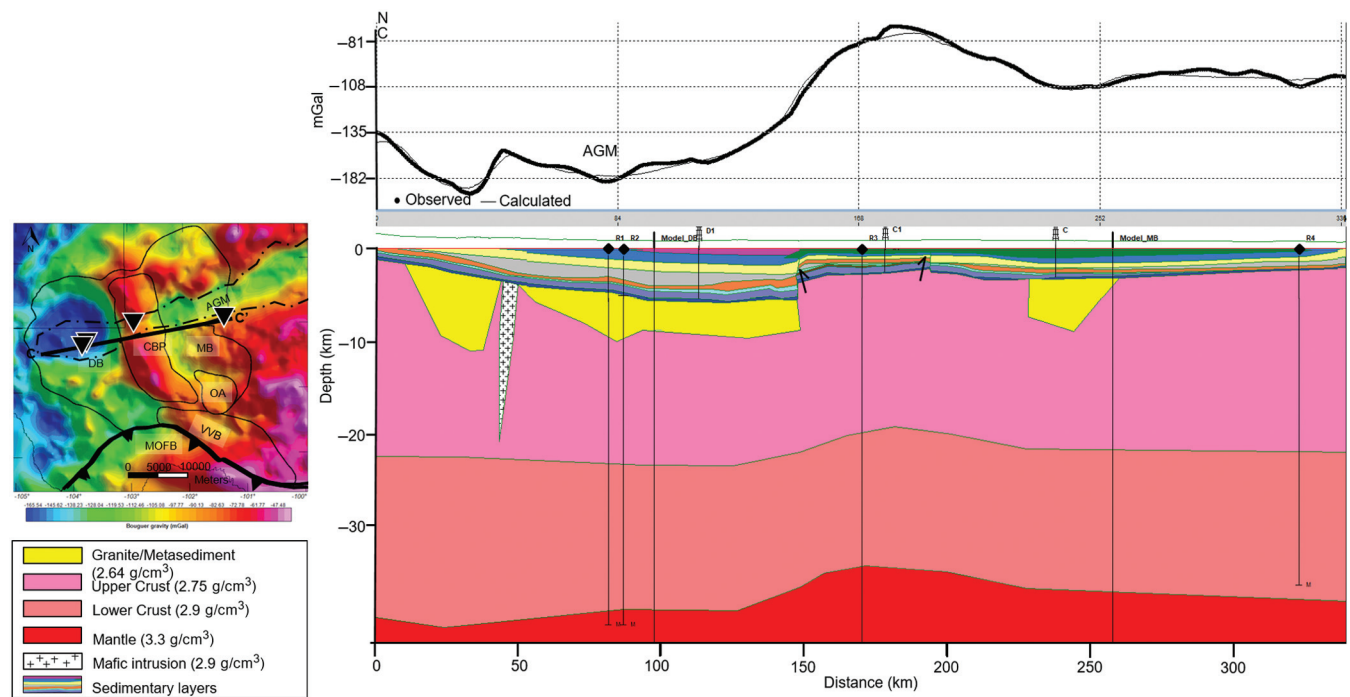


Figure 9. Regional 2D gravity model C-C' trending east-west across the entire northern Permian Basin. The model location is shown on the base map on the left. Four refraction stations are shown as the inverted black triangles on the base map, and they were projected onto the plane of the section to constrain the model along C-C'. The locations of models A-A' and B-B' were tied with model CC'. A mafic intrusion body was added in the east based on the magnetic signal from Figure 5. The Moho depth is deeper beneath the DB and the shallowest in the CBP. The calculated gravity response closely fits the observed gravity signal.

Crustal structure of the Permian Basin

Using gravity data, we completed a 3D structural inversion of the Moho and the lower crust of the Permian Basin. The calculations were iterated until the best fit crustal model was derived. The inverted Moho revealed a deep root underlying the AGM that varies in depth from 5 km beneath the DB to 3 km beneath the CBP and the MB (Figure 12a). Similarly, the top of the lower crust is deepest beneath the AGM, especially in the northern DB (Figure 12b).

We also carried out a density inversion of the upper crust of the Permian Basin. The results suggest that lower density zones exist beneath the AGM that is also observed on our 2D gravity models (Figure 13a). Isolated higher density values correlate with the locations of igneous intrusions mapped by Adams and Keller (1996) (Figure 13a and 13b).

Basin modeling results and implications for hydrocarbon exploration

Basin tectonic phases from subsidence analysis

Subsidence analysis using Petromod 1D was carried out for this study that included sediment decompaction and paleowater depth estimates based on the depositional height of carbonate platform margins, as shown in previous regional cross sections (Feldman and Chairman, 1962; Matchus and Jones, 1984).

Subsidence plots from the wells were divided into five tectonic phases in general agreement with previous subsidence studies (Horak, 1985; Ewing and Christensen, 2016; Ewing, 2019; Ruppel, 2019):

- 1) The **predeformational, Tobosa Basin, and transition phase** extended from the Ordovician to the Early Pennsylvanian with deposition of shallow-marine carbonate facies to deeper marine mudstone facies.

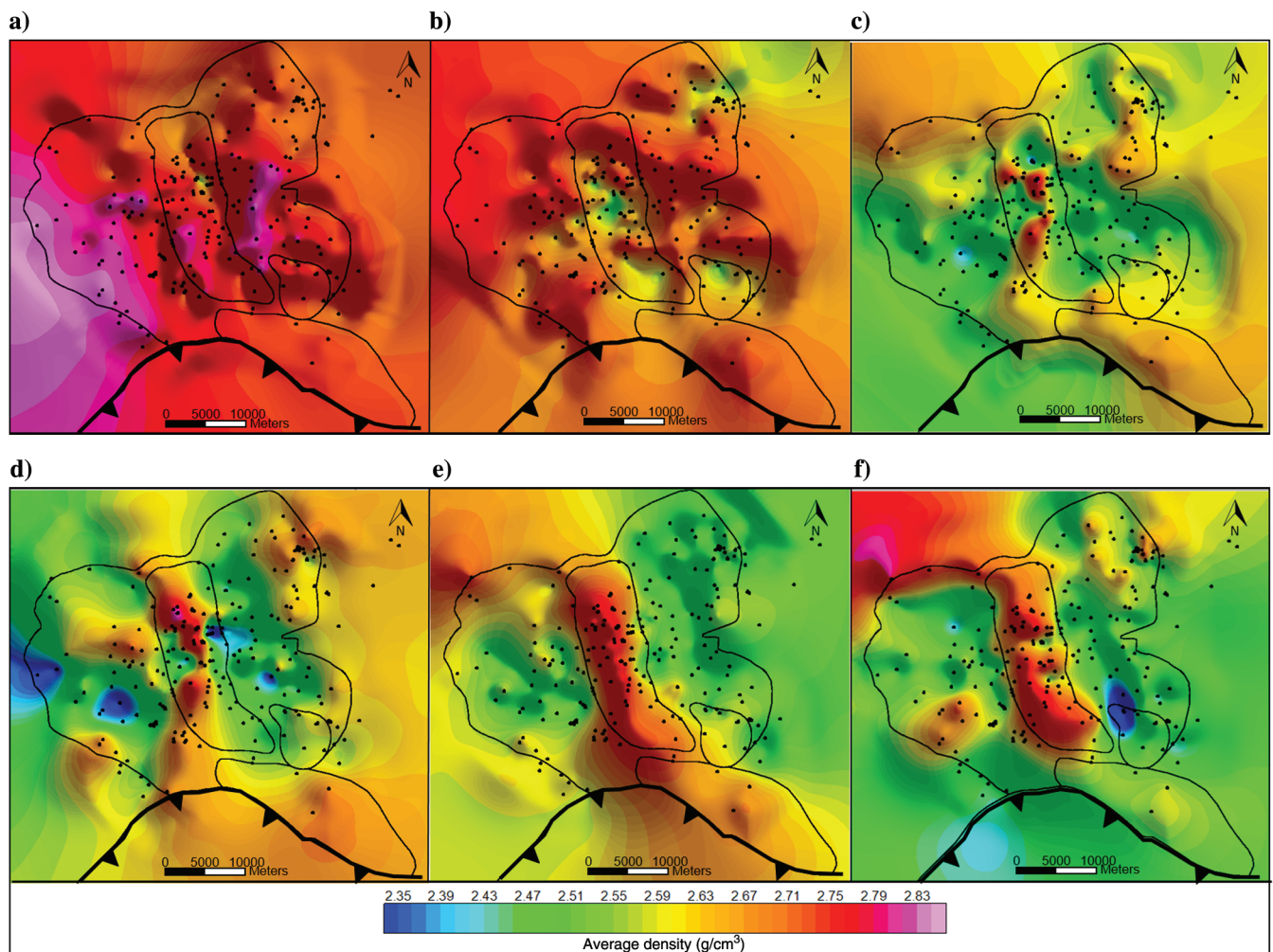


Figure 10. Density grids used for gravity modeling. (a) The average density between the top Ellenburger Formation and the basement. Density values range between 2.83 and 2.78 g/cm³. (b) The average density between the top Devonian Formation and the top Ellenburger. Density values vary from 2.77 to 2.61 g/cm³. (c) The average density between the top Barnett Formation and the top Devonian. Density values vary from 2.67 to 2.50 g/cm³. Density high anomalies were observed on the CBP due to changes in bed thickness affected by the Devonian unconformity. (d) The average density between the top Strawn Formation and the top Barnett. Density values vary from 2.68 to 2.46 g/cm³. (e) The average density between the top Lower Permian Formation and the top Rustler. Density values vary from 2.71 to 2.51 g/cm³. (f) The top Rustler Formation to the top Lower Permian. Density values vary from 2.77 to 2.45 g/cm³. Black dots are the well control points.

- 2) The **main deformational and subsidence phase** extended from the Early Pennsylvanian to the end of the Permian with deposition of mixed, siliciclastic-carbonate deep-marine facies in the basins and shallow-water carbonates facies on the platforms; there are sediment packages up to 2.4 km thick within the basin. Latest Permian (Ochoan) deposits are dominated by evaporites, including more than 1 km of anhydrite and halite in the DB;
- 3) The **postdeformational, low-subsidence phase** occurred during the Triassic with deposition of a thin interval of nonmarine redbeds.
- 4) The **stable platform phase** extended from the Jurassic to the Eocene with significant deposition occurring only during the Cretaceous and represented by shallow marine carbonates and subsidiary clastic rocks. Some minor Laramide deformation effects occurred from the Late Cretaceous to the Middle Eocene;
- 5) The **basin exhumation/tilting phase** occurred from the Late Eocene to the present and was related

to Trans-Pecos volcanism, followed by Neogene Basin and Range extension to the west. This event tilted the western area of the DB, Diablo Platform, and Northwest Shelf to the east, with accompanying erosion of much of the Ochoan and some Guadalupian strata in this area.

Three representative subsidence plots from the MB, DB, and CBP were annotated with the above five tectonic phases, as shown in Figure 14. The subsidence rate was relatively slow (average rate of 13 m/my) in the predeformational phase, Tobosa Basin, and transition phase.

Subsidence history curves show that a marked increase in the subsidence rate occurred during the Early Pennsylvanian as the region entered its main deformational phase and period of maximum subsidence. Subsidence reached its maximum rate (500 m/my in the DB) during the Middle Permian. During the postdeformational phase in the Triassic, the Permian Basin re-

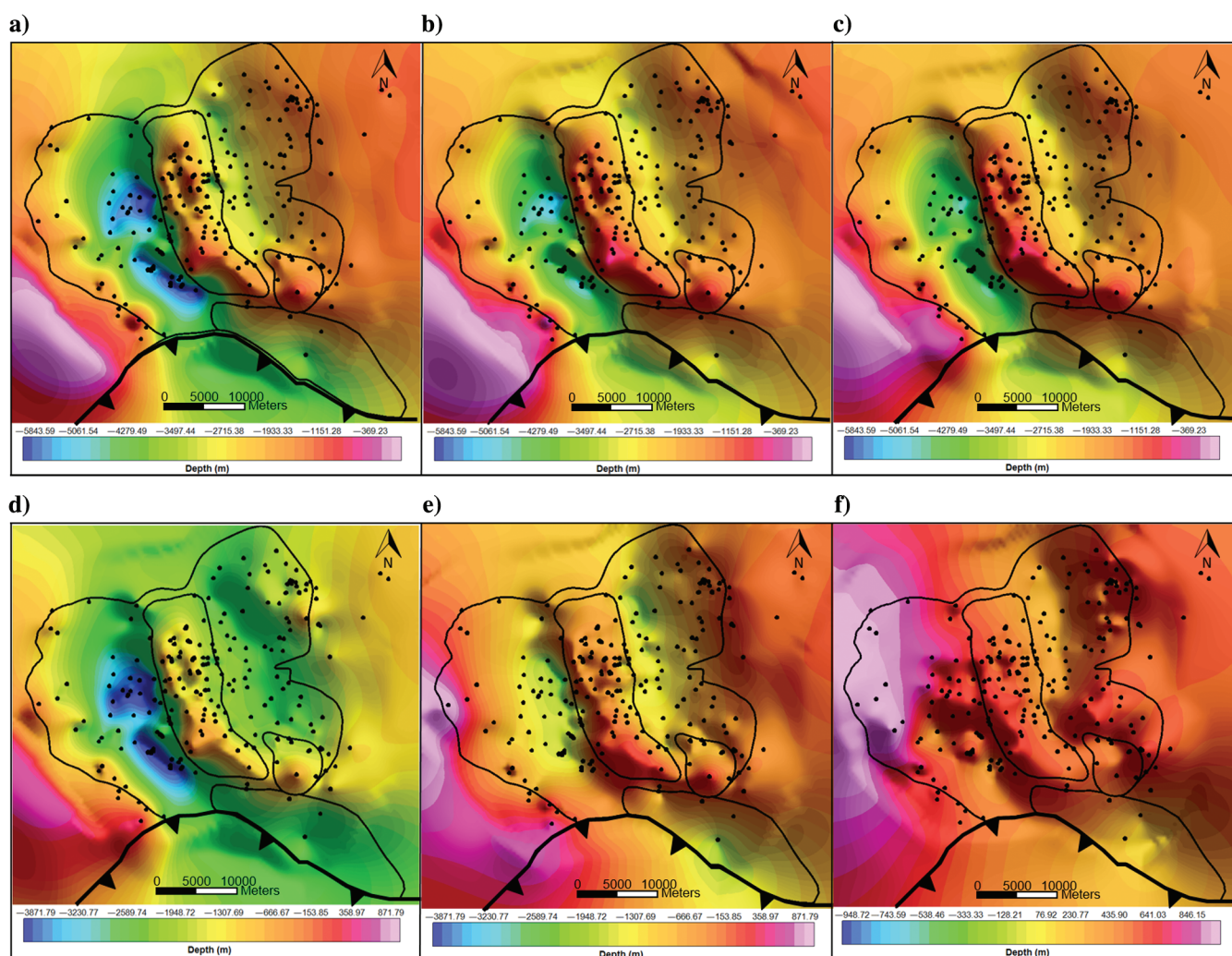


Figure 11. Summary of structural inputs used for gravity modeling. (a) Top Ellenburger Formation, which reaches 6200 m below sea level beneath the central DB (b) Top Devonian Formation. (c) Top Barnett Formation. (d) Top Strawn Formation. (e) Top Lower Permian Formation that was partially eroded across the southern CBP during the Early Permian. (f) Top Rustler Formation. The black dots are the well control points.

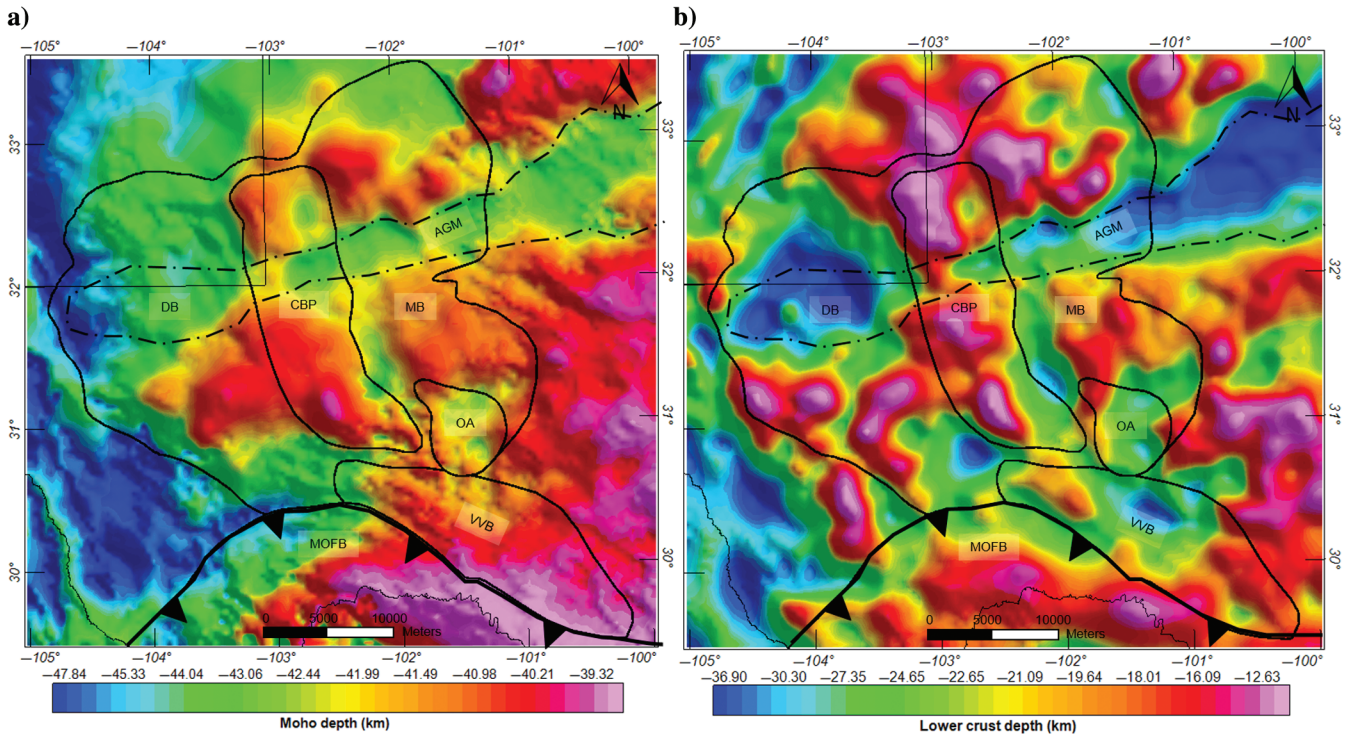


Figure 12. (a) Inverted Moho structure derived from 3D gravity inversion shows a deeper Moho (42.2–45.3 km) beneath the location of the AGM compared to the adjacent areas (38.7–41.8 km). (b) Inverted lower crust structure from 3D gravity inversion shows a deeper lower crust (21.9–36.9 km) beneath the location of the AGM than in the adjacent areas (10.9–21.4 km).

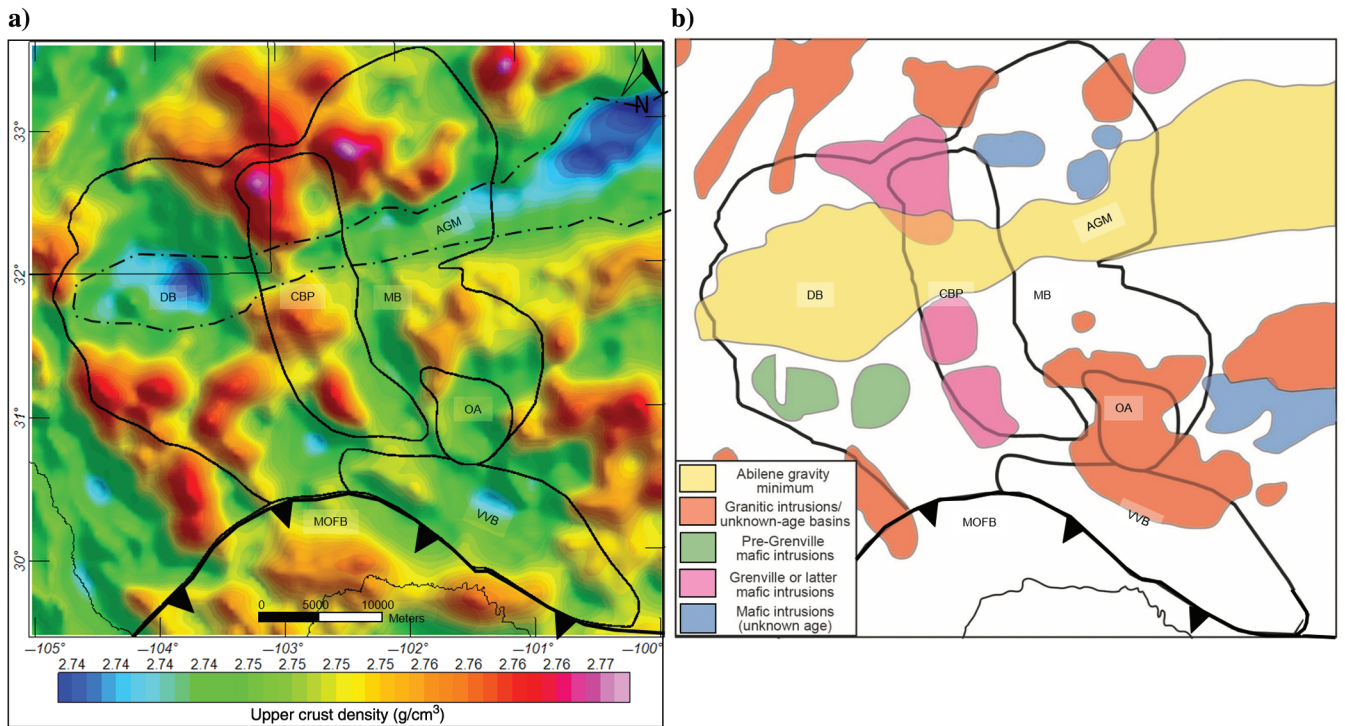


Figure 13. (a) Summary of the density inversion results for the upper crust. The density value distribution shows a linear density low in the upper crust at the location of the AGM, which closely matches the 2D gravity results. (b) Basement geology of the Permian Basin study area (modified from Adams and Keller, 1996) showing major basement features labeled in Figure 1. Locations of igneous intrusion in panel (b) correlate with density highs in a.

gion underwent minor subsidence at a rate of 0–2 m/my.

Subsidence decreased abruptly during the Triassic and remained stable during the stable platform phase. After the post-Paleozoic stabilization of the region, subsidence was only punctuated by uplift during the late Cretaceous-Eocene Laramide Orogeny and later during the Miocene to recent basin and range extensional event.

Stratigraphy of units deposited during the five tectonic events

Lithologic components vary laterally between the CBP and the flanking DB and MB during the main deformational phase from Early Pennsylvanian to Late Permian (Galley, 1958; Adams, 1965; Ruppel, 2019) (Figure 2).

The CBP is a late Paleozoic carbonate platform dominated by limestone and dolomite. The main sediment packages of the DB are composed of fine-grained mudstone with interbedded sandstone (approximately 20%), whereas the sediment packages in the MB consist of more limestone (approximately 15%) and sandstone

(approximately 30%) with minor shale (Matchus and Jones, 1984). These sediment packages are bounded by high-angle thrust faults active during periods of maximum thrusting occurring in the Pennsylvanian and especially during Wolfcampian time (Figure 2). Up to 1000 m of erosion or nondeposition was observed on the CBP as a result of uplift along the bounding thrust faults while the adjacent DB and MB were undergoing rapid subsidence (Figure 2). Tectonic activity in this region decreased greatly following the Late Permian (Guadalupian) and ceased by the end of the Permian (Ewing, 2019).

Distribution of thermal maturity with respect to Permian Basin depocenters

Thermal maturity was modeled at the same locations as the wells that were used for subsidence analysis (Figure 15). The maturity profile was calibrated with corrected bottom-hole temperature data from Southern Methodist University geothermal laboratory database and vitrinite reflectance data from the USGS database (Pawlewicz et al., 2005). It should be noted that alter-

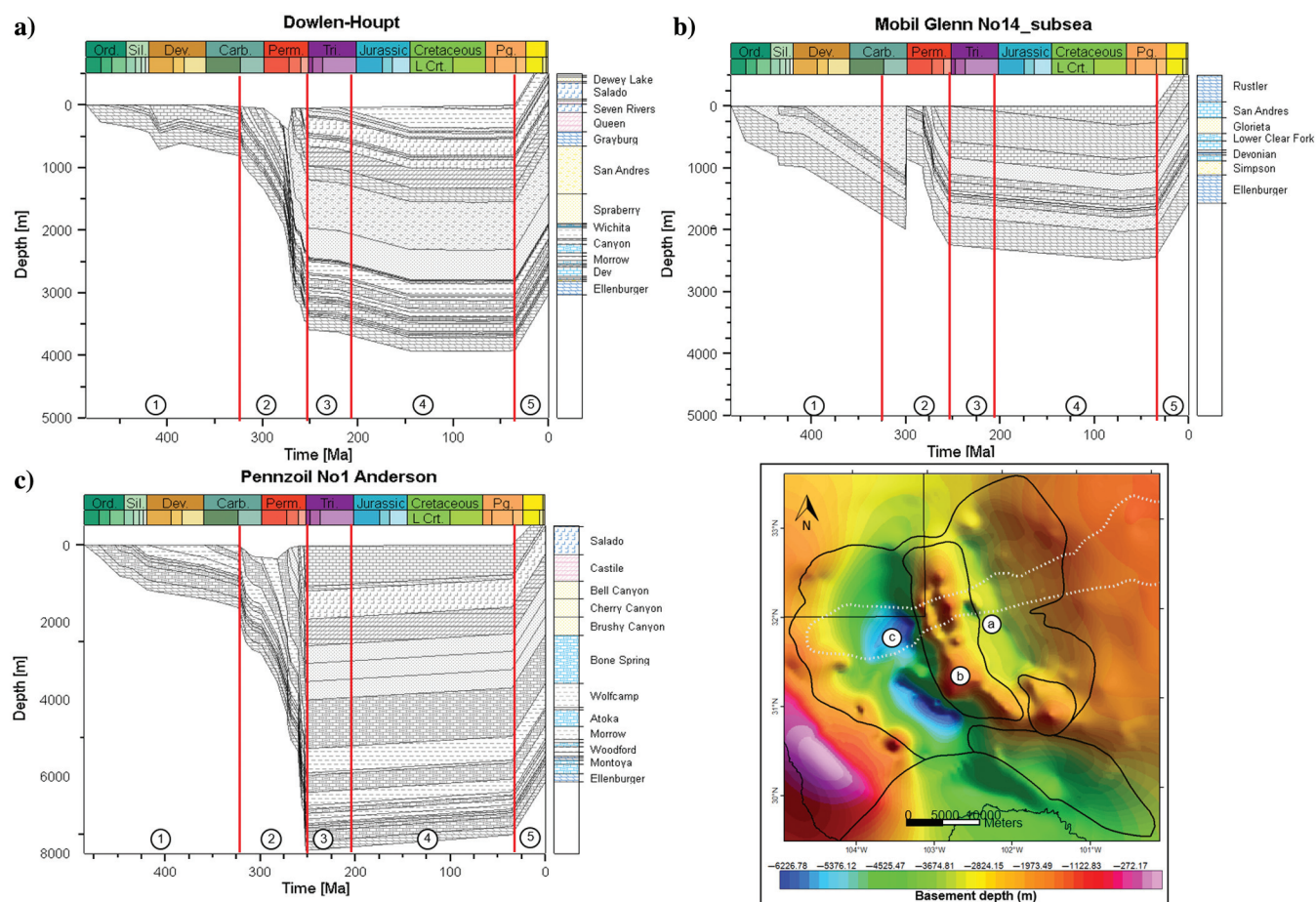


Figure 14. Subsidence history with five numbered tectonic stages from the Cambrian through Neogene based on representative exploration wells for (a) MB — Dowlan-Haupt No. 1 well, central Midland county; (b) CBP — Mobil Glenn No. 14 well, southern Crane county, and (c) the DB — Pennzoil No. 1 Anderson well, central Loving County. Five tectonic phases include the (1) pre-deformational Tobasa Basin and transition phase, (2) main deformational phase; (3) postdeformational, subsidence phase, (4) stable platform phase, and (5) basin reactivation phase.

nate measures of maturity by [Manos and Perez \(2018\)](#) using Raman spectroscopy yielded different results for the Permian Basin than the maturity results that we present here. Our basin modeling assumed constant heat flow over geologic time, and the heat-flow information was based on the regional geothermal map of North America ([Blackwell and Richards, 2004](#)). Two major hydrocarbon source rocks focused in this study are the Wolfcamp shale and the Woodford shale.

In general, the DB is more thermally mature than the MB. The CBP lies within the immature zone due to less burial and a large amount of uplift and erosion during the Early Permian (Figure 2). In the DB, the maturity profile indicates that the top and base of the Woodford shale lies in the overmature zone with thermal maturity higher than 2%Ro (Figure 15a). The Wolfcamp shale is partially in the oil window and partially in the gas window (Figure 15a). In contrast, in the southern CBP, the Wolfcamp shale is in the immature zone while the Woodford shale was eroded below during the Lower Permian unconformity (Figure 15b). In the MB, most of the Wolfcamp shale and the Woodford shale is currently in the oil

window with Ro values ranging from 0.5% to 1.5% (Figure 15c).

Discussion

Reconciling contrasting views on the regional, tectonic controls of Permian Basin subsidence

Earlier interpretations of the Ouachita-Marathon-Sonoran orogenic belt by [Graham et al. \(1975\)](#), [Kluth et al. \(1981\)](#), and [Dickinson and Lawton \(2003\)](#) emphasized its diachronous, east-to-west progression during the Pennsylvanian and Permian and its tectonic control on a near-field, elongate, suture-parallel foreland basin adjacent to a thin-skinned, northward-vergent fold-thrust belt ([Hickman et al., 2009](#)). [Kluth et al. \(1981\)](#) propose the modern India collision with central Asia as an analog for the far-field deformation effects of the ARM triggered by the Ouachita-Marathon-Sonoran orogenic belt.

A later generation of geoscientists that includes [Marshak et al. \(2000\)](#) and [Craddock et al. \(2017\)](#) recognized many far-field structural effects in the North American craton. These late Paleozoic structures were

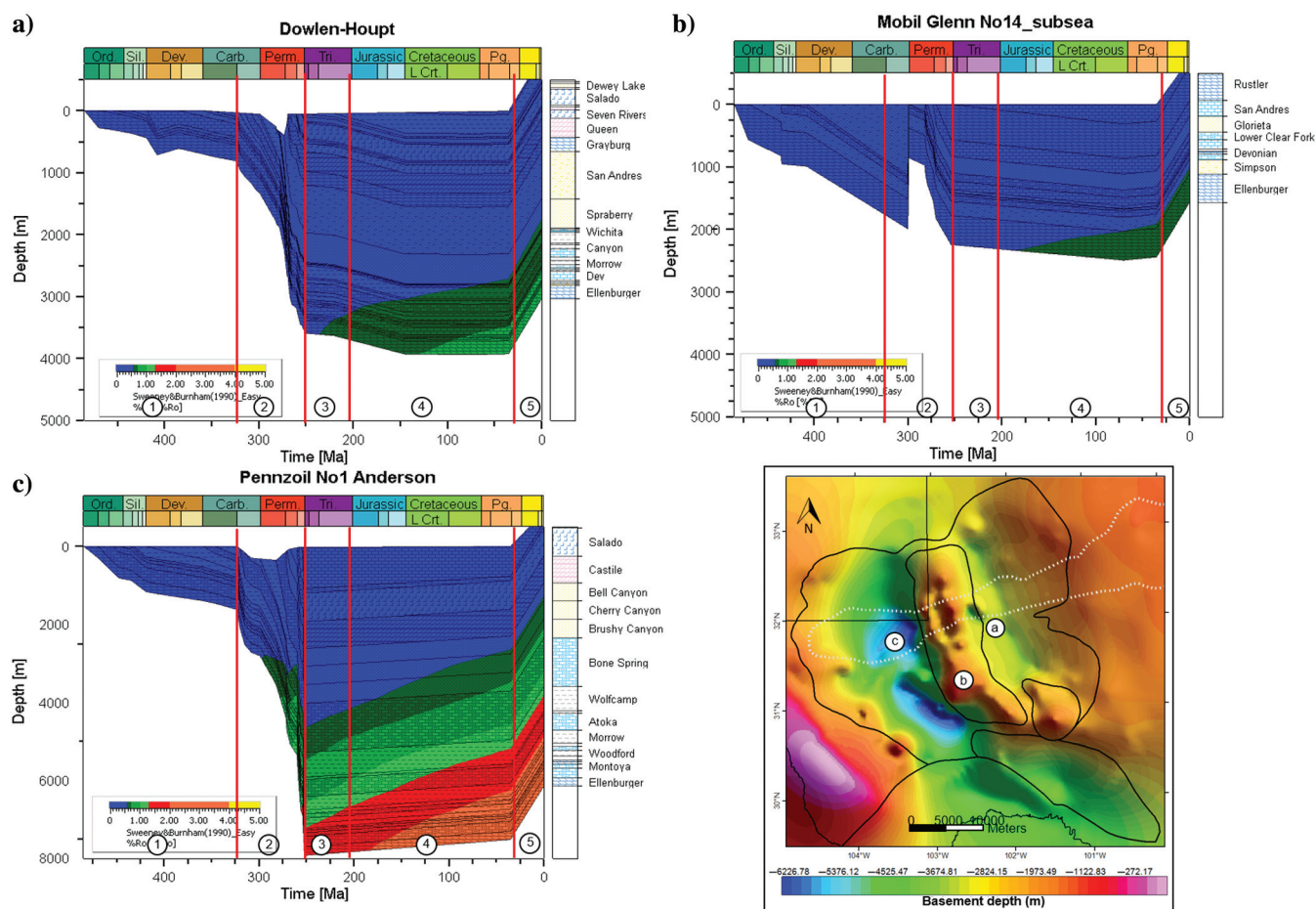


Figure 15. Maturity modeling based on representative exploration wells for (a) MB — Dowlen-Houpt No. 1 well, central Midland county, (b) CBP — Mobil Glenn No. 14 well, southern Crane county, and (c) the DB — Pennzoil No. 1 Anderson well, central Loving county. Major hydrocarbon source rocks in the MB have entered the oil window. In the DB, major source rocks are partially in the oil window whereas deeper source rocks, such as the Woodford shale, have entered the gas window. Major source rocks are mostly immature in the shallowly buried and partially eroded CBP.

attributed to a single or slightly varying, north–south, Ouachita-Marathon-Sonora stress field that reactivated and inverted intracratonic features of the ARM and areas as distant as the upper Midwest that included Precambrian rifts and older, orogenic belts. Marshak et al. (2000) propose that strike-slip faulting was a common mode of reactivation of these older structures that included Precambrian faults, rifts, and suture zones.

In a more recent revision of these earlier ideas of far-field, late Paleozoic deformational effects, Leary et al. (2017) and Ewing (2019) point out that the orientation of north–south basement uplifts that comprise the widespread ARM orogenic event is oriented at right angles to the compression direction of the Ouachita-Marathon-Sonoran orogeny and are better explained by a uniform, northeast-directed compression related to orogenic shortening events along the Pacific margin of North America. Therefore, the northwest- or north-directed shortening related to the Ouachita-Marathon-Sonora event was a less significant “soft orogeny” in comparison to the “harder” northeast-directed Pacific orogenies (van Staal and Zagorevski, 2020).

One concept that can help reconcile these differing views of the structural controls of the late Paleozoic Permian Basin is the concept of a contiguous versus broken foreland basin, as illustrated in active foreland basins along the Andean margin of South America (Strecker et al., 2011). *Contiguous foreland basins* are those formed adjacent to a fold-and-thrust belt and result from accommodation space created by the flexural response of the crust to the topographic load of the fold-and-thrust belt, such as the Arkoma Basin and the Fort Worth Basin. This leads to the familiar suite of contiguous foreland basin depozones: the wedge-top, foredeep, forebulge, and backbulge (DeCelles and Gilles, 1996). Contiguous foreland basins in the northern Andes form in a retroarc position adjacent to areas of steeper subduction and extensional type arcs (Strecker et al., 2011).

In contrast, *broken foreland basins* are formed in areas of flat subduction and compressional type arcs where retroarc convergence is accommodated along reactivated, high-angle structures in the basement. Uplift along these reactivated basement structures is disparate in space and time and create ranges and basins that are limited in their along-strike length and occur far inboard and remote from the main topographic and deformation front of the orogen. These broken foreland basins tend to be isolated and restricted from one another and are quite different in appearance from the more familiar and much larger, contiguous foreland basins (Strecker et al., 2011).

The Permian Basin as a broken foreland basin

Although the Permian Basin lies less than 100–400 km north of the Marathon thin-skinned, fold, and thrust belt (Hickman et al., 2009), its main depocenter is oriented at right angles to the Marathon thrust front orientation. Galley (1958, 1970) propose that this unusual orientation is related to the reactivation of a Precambrian rift formed

at approximately 1100 Ma and later reactivated during the Marathon orogeny and the formation of the ARM. These north–south rift trends are not easily mapped on potential field data because the Permian Basin is cross-cut by the east–northeast-trending AGM that we have described in this paper (Figure 4). We also noted rapid gravity changes along the boundaries among the AGM, CBP, and flanking two subbasins.

Along with Adams and Keller (1994, 1996) and Keller (2019), we have focused on the reactivation of the regional crustal feature marked by the AGM. Major basement-involved structures have been repeatedly activated during subsequent plate collisions and rifting events (Kluth et al., 1981; Marshak et al., 2000; Craddock et al., 2017; Snee and Zoback, 2018). As shown in Figure 16a, several regional-scale faults are known to exist in the Permian Basin region (Walper, 1977; Shumaker, 1992; Yang and Dorobek, 1995; Ewing, 2019). One prominent feature is the east–west-striking left-lateral strike-slip Grisham fault (GF) along the southern margin of the AGM that was active during the period of maximum Permian subsidence, as shown on the Permian thickness map (Shumaker, 1992; Ewing, 2019; Ruppel, 2019) (Figure 16b). This east–northeast-trending basement ridge defined on its northern edge by the GF is roughly parallel to the northernmost salient of the Marathon fold and thrust belt 100 km to the south. For a strike-slip fault, this is an unexpected orientation for reactivation invoking north–south shortening associated with the Marathon orogeny. Leary et al. (2017) and Ewing (2019) propose that the GF reflects a northeast–southwest shortening that could be the composite response to the Marathon, Sonoran, and Nevadan belts. In addition to the GF, two other strike-slip fault zones (Big Lake, Todo-Elk-horn) mapped by Ewing (2019) are shown in Figure 16a. Moreover, the CBP itself shows three left-lateral deflections in its overall north–south trend (Figure 16a). The central and northern CBP was bound by the northwest–southeast-trending Monahans and the Hobbs transverse zone, respectively, as discussed by Ewing (2019)

Deformational model for the rift inferred along the AGM trend

We propose that the underlying crustal structure of the AGM also plays an important role in generating the large amount of subsidence observed during the Marathon and ARM orogenic events. We propose that the elongate mixture of granitic and metasedimentary rocks with a lower density as interpreted from gravity modeling (Figures 7, 8, 9, and 13a) – acted as a zone of weakness that collapsed and focused extreme synorogenic subsidence (phase 2, Figure 14). Synorogenic deformation included left-lateral shearing along the GF that coincides with the east–northeast-trending southern edge of the AGM (Figure 16a). It should be noted that this local east–west-trending basement low adjacent to the GF is a second-order effect, with the primary DB depocenter remaining in a north–south orientation.

As a result of Permian shortening, the crust and upper mantle of the AGM, which we infer as a Precambrian rift feature — similar to those described by Marshak et al. (2000) or as proposed by Mosher (1998) — were depressed along the rift-controlled, preexisting zone of weakness, as illustrated in Figure 16c. An analog of the response of the lithosphere under compression along a preexisting weakness zone has been described from the eastern North Sea by Gemmer et al. (2002) (Figure 7). The results from our gravity structural inversion further confirmed that the depths to the lower crust and Moho are deeper below the AGM (Figure 13).

Analysis of regional burial history pattern

We compiled subsidence analysis representative wells of seven sedimentary basins along the Marathon-Ouachita orogenic belt and part of the ARM system that include from east to west: (1) the Arkoma Basin, (2) the Ana-

darko Basin, (3) the Palo Duro Basin, (4) the Val Verde Basin (VVB), (5) the MB, (6) the DB, and (7) the Orogande Basin to analyze the subsidence pattern on a regional scale (Figure 17a and 17d). We measured the distance between each geohistory site and from the western edge of the Black Warrior Basin, where the continental collision is thought to have begun (Graham et al., 1975; Dickinson and Lawton, 2003).

In Figure 17b, we plotted the measured distance versus the average subsidence rate during the period of maximum subsidence during the Pennsylvanian-Permian orogenic period and the total subsidence for the seven basins. The basins with the higher average subsidence rates from east to west are the Arkoma Basin (135 m/my), Anadarko Basin (152 m/my), VVB (123 m/my), and DB (113 m/my). With the exception of the Anadarko Basin, these higher rate basins are within 150 km of the Ouachita-Marathon deformation

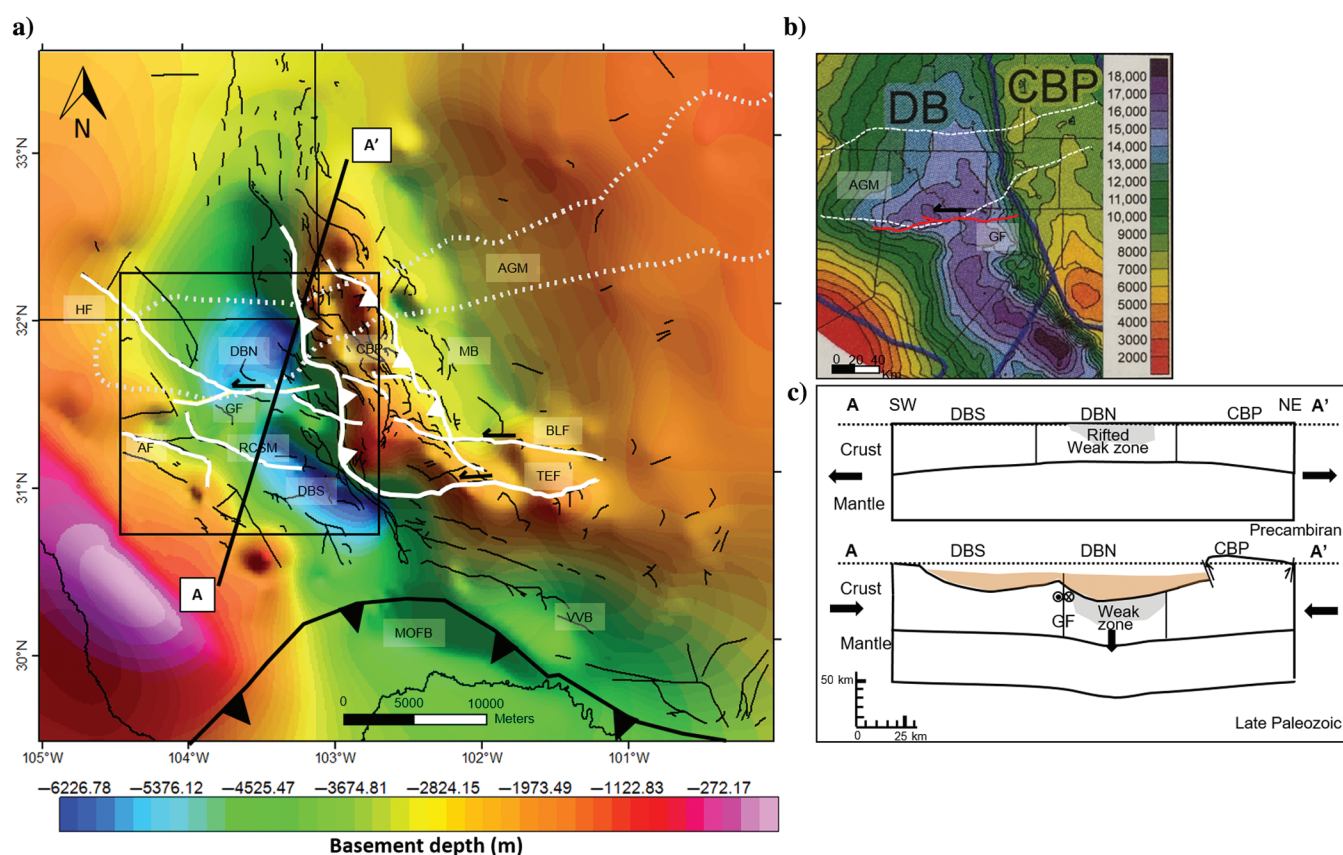


Figure 16. (a) Comparison of Paleozoic faults distribution (the thin black lines) with mapped by Ruppel et al. (2008) and Ewing (2019) and the AGM (the white dotted line). Major northwest–southeast-trending faults are marked as the white lines. Major thrust faults are the boundary of the CBP marked by the thick, white line. The black box shows the location of (b). DBN, North Delaware Basin; DBS, South Delaware Basin; BLF, Big Lake fault; TEF, Todd-Elkhorn fault; GH, Grisham fault; HF, Huapache fault; AF, Apache fault; and RCSM, Rojo Caballos-San Martine fault zone. (b) Thickness of Permian rocks (as measured from the base Permian to the surface) in the DB. Grisham left-lateral strike-slip fault is shown by the red line (modified from Ruppel, 2019). The AGM is shown by the white dashed polygon. (c) Conceptual model for convergence of the crustal structure with a pre-existing, rifted zone of weakness (modified from Gemmer et al., 2002). The model shows the crust and mantle response to east–west compression during the phase 2 main deformational phase from the Early Pennsylvanian to the Late Permian. The rifted zone of weakness (AGM) acts as a load that presses down the region adjacent to the weak zone due to the lateral strength in the crust and mantle. The location of the modeled line is labeled in panel (a). GF, Grisham fault.

front. The more distant basins except for the DB (the Palo Duro Basin — 480 km and the Orogrande Basin — 440 km) show lesser average subsidence rates (49 and 47 m/my, respectively) and total sedimentation (Figure 17b). The DB shows the highest total subsidence of 8000 m as it continued to subside at a high subsidence rate up to the end of the Permian.

In Figure 17c, we plotted the measured distance versus the start and end times for the most rapid period of the presumed climax of orogenic activity — along with the end time for all orogenic activity — for the seven basins. These plots show a slight younging trend from east to west over the 1000 km distance with an average rate of 0.04 cm/yr. This rate is considerably less than the rate of 0.6 mm/yr that we calculated using the data provided by Leary et al. (2017).

Our younging rate is similar to the rate of 0.02 mm/yr that we calculated using data provided by Ewing (2019). Our data indicate that the South America-Yucatan collision occurred almost synchronously along the Ouachita-Marathon thrust front, and, for that reason, higher sedimentation occurred in the more proximal basins as a consequence of an elevated highland generated along this zone (Gao et al., 2019; Liu and Stockli, 2020; Soto-Kerans et al., 2020).

Effect of basement structure on the thermal maturity of source rocks

The top to basement depth shown in Figure 18a was constrained by gravity modeling, well logs, and previous subsurface mapping summarized by Ruppel (2008). Two depocenters were observed in the northwest and

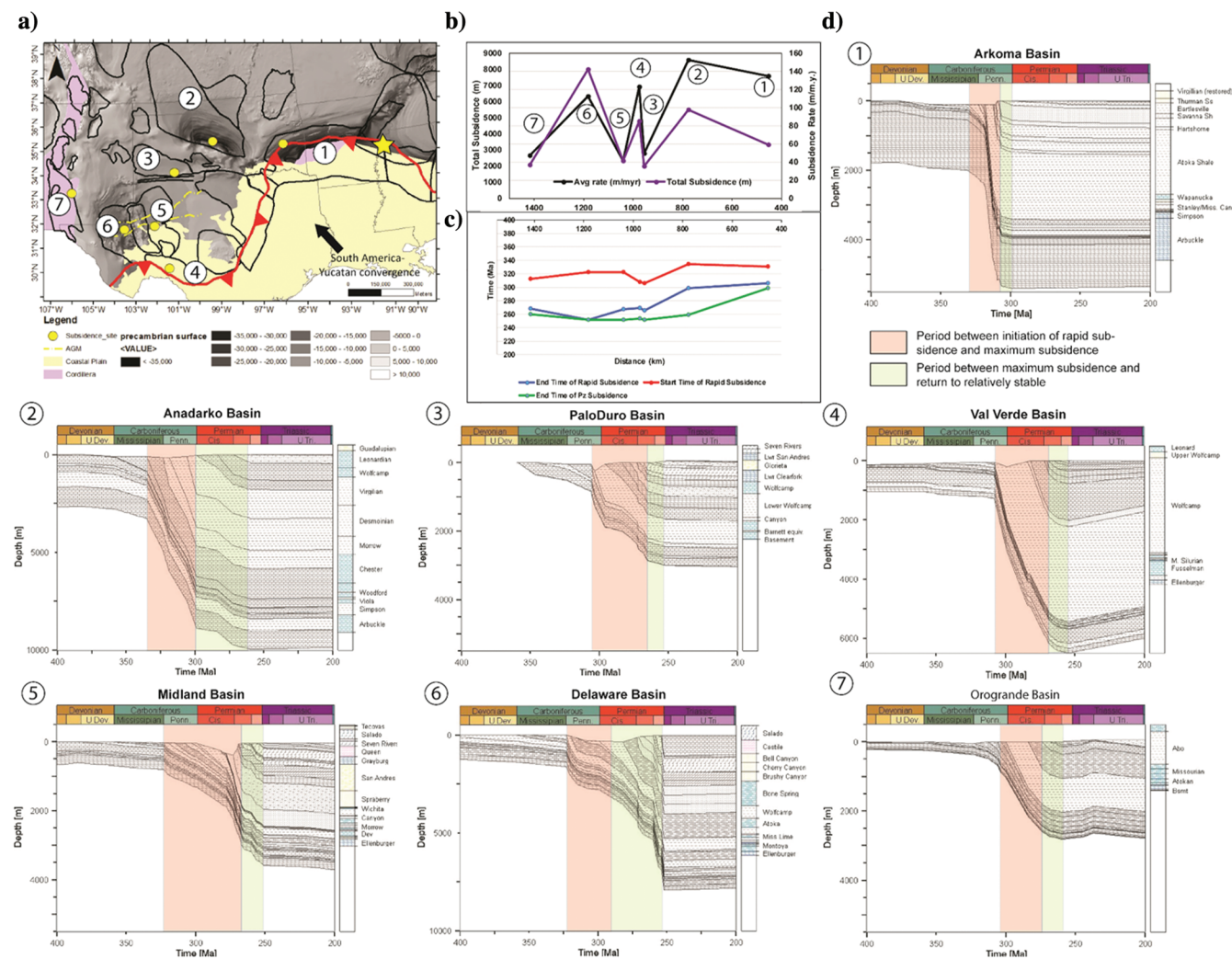


Figure 17. (a) Location of the representative wells of seven sedimentary basins along the Marathon-Ouachita orogenic belt and part of the ARM system, including the (1) Arkoma Basin, (2) Anadarko Basin, (3) Palo Duro Basin, (4) VVB, (5) MB, (6) DB, and (7) Orogrande Basin. The basement was modified from Marshak et al. (2017). (b) Plot showing the maximum subsidence rate for the seven basins compared to their estimated distance from the easternmost location where continental collision is thought to have begun (labeled as a star). (c) Plot showing the time of the most rapid subsidence initiation and the time of maximum subsidence rate for the seven basins versus estimated distance away from the location where continental collision began (labeled in start). (d) Subsidence analysis for the seven basins marked with the period from the initiation of rapid subsidence to reaching their maximum subsidence rate followed by the end of rapid subsidence and with an eventual return to basin stability.

southeast DB (Figure 18a). The depocenter in the northern DB is called the Malaga subbasin by Ewing (2019). The depocenter in the northern DB overlies the east–northeast trend of the AGM and is bounded in the south by the GF (Figure 18a).

Basement depth was then compared with thermal maturity and production trend in this region. We combined our maturity modeling results with previous maturity studies in the Permian Basin to generate a maturity map of top Devonian (modified from Echegu, 2013; Jarvie et al., 2017). The maturity map shows that the dry gas window, which has the highest thermal maturity, correlates with the thicker depocenters in the DB (Figure 18b). The location of maturity associated with the deeper depocenters also correlates with the most recent production trends in the Permian Basin unconventional plays (Figure 18c). Thermal maturity is also related to the presence of granitic/mafic intrusion bodies, which will produce higher heat flow. The study by Manos and Perez (2018) using

Raman spectroscopy of carbonaceous material shows that the highest maturity gradient lies in an area of higher heat flow in the southwestern DB in western Pecos County, that they attribute to the area of Cenozoic intrusions. The location of the highest maturity gradient also correlates with the presence of two major bodies of pre-Grenville mafic intrusions (Adams and Keller, 1996; Manos and Perez, 2018), as shown in Figure 13a.

Production information from Enverus shows that from December 2019 to February 2020, new wells started to produce in a concentrated area in the northwestern DB that correlates with these areas of more mature basement depocenters (Figure 18c). The DB has been the site of recent large increases in unconventional hydrocarbon production, especially from the Wolfcamp and Bone Spring formations. Although reservoir characteristics are the primary driver, we speculate that thicker sediments and higher thermal maturity may have contributed to this sweet spot of recent oil production.

Conclusion

We have developed three regional 2D gravity models that incorporate the following data sources: (1) density and lithologic controls from industry well logs drilled to the Ordovician Ellenburger Formation, (2) published seismic refraction data, and (3) published, regional cross sections in the Permian Basin. Because sediment densities and basinal stratigraphy vary between the three components of the Permian Basin — MB, DB, and CBP — we divided the sedimentary section above the crystalline basement into seven layers for the 2D model. The result of this gravity modeling improved the boundaries of a 34–108 km wide, 650 km long east–west-trending AGM over the northern Permian Basin, which we infer is underlain by a belt of Early Mesoproterozoic, granitic, and metasedimentary rocks with a lower density compared to the surrounding areas of the upper crust.

We also generated a 3D model incorporating structural and density controls from well logs. Structural inversion results show that the depth to top lower crust and Moho is deeper below the AGM, especially beneath the deep depocenter of the northern DB. Density inversion results further confirm that the upper crust density is lower beneath the AGM.

Subsidence analysis-based deep wells in the Permian Basin allow division of the stratigraphic section into five tectonic phases:

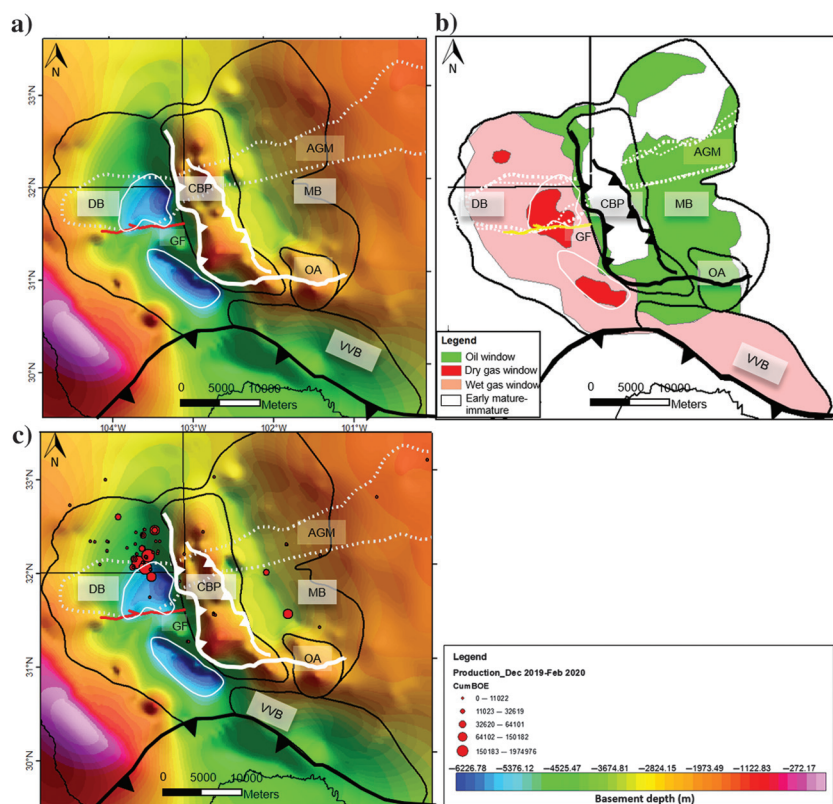


Figure 18. (a) Depth to basement map constrained by the gravity model, the well logs, and the previous study by Ruppel (2008). Two depocenters were observed in the DB (in the white polygon). (b) Top Devonian maturity map modified from Echegu (2013) and Jarvie et al. (2017) showing the distribution of the oil window, wet gas window, dry gas window, and areas that are early mature to immature. Zones of basement depocenters from (a) are shown in the white polygons. (c) Basement structure with production wells for a three-month period (Dec. 2019–Feb. 2020) based on data provided by Enverus. New wells that start production with a promising barrel of oil equivalent (BOE) concentrated in the northern DB. Zones of basement depocenters from (a) are shown in the white polygons.

- 1) predeformational, Tobasa Basin and the transition phase from the Ordovician to the Early Pennsylvanian
- 2) main deformational and subsidence phase from the Early Pennsylvanian to the Late Permian
- 3) postdeformational, low-subsidence phase from the Late Permian to the Late Triassic
- 4) stable platform phase from the Jurassic to the Eocene
- 5) basin exhumation/tilting phase from the Late Eocene to the present.

The maximum subsidence (up to 421 m/my) happened during the main deformational phase with sediment packages up to 2.4 km thick.

We propose that the belt of granitic and metasedimentary rocks inferred from gravity modeling acted as a zone of preferential weakness in a broken foreland basin setting that accommodated regional shortening related to the Marathon orogeny to the south and to coeval orogenies along the Sonoran margin to the southwest and the Nevadan margin to the west. Basement depth in the Permian Basin defines the limits of deep basinal areas that may host the most productive and thermally mature source rock kitchens. These deep and localized depocenters are controlled in part by Permian strike-slip faults aligned with the edges of the AGM. High-maturity zones for hydrocarbons overlie deeper basement depocenters and are delineated by our basement maps. The deeper (4.2–6.2 km) basement of the DB has resulted in its broader zone of oil and gas maturity than observed above the shallower (1.6–3.6 km) basement of the MB.

Acknowledgments

We thank Enverus and TGS for kindly providing the well-log data used in this study and Seequent/Geosoft for providing the educational license of the Oasis montaj software that was used for the gravity modeling. We thank J. Keay, L. Sternbach, and C. Sternbach for their help in data searching. We thank the industry sponsors of the Conjugate Basins, Tectonics, and Hydrocarbons consortium at the University of Houston for their continuing support. Special thanks go to T. E. Ewing, N. Perez, L. (Tingwei) Ko, and M. Khatiwada for their constructive reviews of the manuscript.

Data and materials availability

Data associated with this research are confidential and cannot be released.

References

- Adams, D. C., and G. R. Keller, 1994, Possible extension of the Midcontinent Rift in west Texas and eastern New Mexico: *Canadian Journal of Earth Sciences*, **31**, 709–720, doi: [10.1139/e94-063](https://doi.org/10.1139/e94-063).
- Adams, D. C., and G. R. Keller, 1996, Precambrian basement geology of the Permian Basin region of West Texas and eastern New Mexico: A geophysical perspective: *AAPG Bulletin*, **80**, 410–431, doi: [10.1306/64ED87FA-1724-11D7-8645000102C1865D](https://doi.org/10.1306/64ED87FA-1724-11D7-8645000102C1865D).

- Adams, D. C., and K. C. Miller, 1995, Evidence for late Middle Proterozoic extension in the Precambrian basement beneath the Permian Basin: *Tectonics*, **14**, 1263–1272, doi: [10.1029/95TC02317](https://doi.org/10.1029/95TC02317).
- Adams, J. E., 1965, Stratigraphic-tectonic development of Delaware Basin: *AAPG Bulletin*, **49**, 2140–2148, doi: [10.1306/A6633888-16C0-11D7-8645000102C1865D](https://doi.org/10.1306/A6633888-16C0-11D7-8645000102C1865D).
- Blackwell, D. D., and M. Richards, 2004, Geothermal Map of North America dataset: AAPG, Tulsa, Oklahoma, <https://www.smu.edu/Dedman/Academics/Departments/Earth-Sciences/Research/GeothermalLab/DataMaps/GeothermalMapofNorthAmerica>, accessed 10 December 2019.
- Blakely, R. J., 1995, *Potential theory in gravity and magnetic applications*: Cambridge University Press.
- Craddock, J., D. Malone, R. Porter, J. Compton, J. Luczaj, A. Konstantinu, J. Day, and S. Johnston, 2017, Paleozoic reactivation structures in the Appalachian-Ouachita-Marathon foreland: Far-field deformation across Pangea: *Earth-Science Reviews*, **169**, 1–34, doi: [10.1016/j.earscirev.2017.04.002](https://doi.org/10.1016/j.earscirev.2017.04.002).
- Daniels, V. B., C. A. Patricia, H. R. Mark, P. C. Victoria, R. S. Ronald, S. J. Phillips, and J. D. Ravat, 2002, Digital data grids for the magnetic anomaly map of North America, <https://mrdata.usgs.gov/magnetic/>, accessed 5 January 2019.
- DeCelles, P. G., and K. A. Giles, 1996, Foreland basin systems: *Basin research*, **8**, no. 2, 105–123.
- Dickinson, W. R., and T. F. Lawton, 2003, Sequential intercontinental suturing as the ultimate control for Pennsylvanian Ancestral Rocky Mountains deformation: *Geology*, **31**, 609–612, doi: [10.1130/0091-7613\(2003\)031<0609:SISATU>2.0.CO;2](https://doi.org/10.1130/0091-7613(2003)031<0609:SISATU>2.0.CO;2).
- Djeddi, R., 1979, An integrated geophysical and geological study of the deep structure and tectonics of the Permian basin of west Texas and southeastern New Mexico: M.S. thesis, University of Texas at El Paso.
- Dumas, D. B., 1982, Seismicity of west Texas: Ph.D. thesis, The University of Texas at Dallas, 1–94.
- Dutton, S. P., E. M. Kim, R. F. Broadhead, C. L. Breton, W. D. Raatz, S. C. Ruppel, and C. Kerans, 2004, Play analysis and digital portfolio of major oil reservoirs in the Permian Basin: Application and transfer of advanced geological and engineering technologies for incremental production opportunities, 1–428, <https://www.osti.gov/servlets/purl/828411>, accessed 15 January 2019.
- Dutton, S. P., E. M. Kim, R. F. Broadhead, W. D. Raatz, C. L. Breton, S. C. Ruppel, and C. Kerans, 2005, Play analysis and leading-edge oil-reservoir development methods in the Permian Basin: Increased recovery through advanced technologies: *AAPG Bulletin*, **89**, 553–576, doi: [10.1306/12070404093](https://doi.org/10.1306/12070404093).
- Echegu, S., 2013, Geological and geochemical investigation of the petroleum systems of the Permian Basin

- of West Texas and Southeast New Mexico: Ph.D. thesis, University of Houston, 1–195.
- Ewing, T. E., 2019, Tectonics of the West Texas (Permian Basin) — Origins, structural geology, subsidence, and later modification, *in* S. C. Ruppel, ed., *Anatomy of the Paleozoic basin: The Permian Basin, USA* (vol.1, ch. 3): The University of Texas at Austin, Bureau of Economic Geology Report of Investigations 285: AAPG Memoir, **118**, 63–96.
- Ewing, T. E., M. A. Barnes, and R. E. Denison, 2019, Proterozoic Foundations of the Permian Basin, West Texas and Southeastern New Mexico — A review, *in* S. C. Ruppel, ed., *Anatomy of the Paleozoic basin: The Permian Basin, USA* (vol. 1, ch. 3): The University of Texas at Austin, Bureau of Economic Geology Report of Investigations 285: AAPG Memoir, **118**, 63–96.
- Ewing, T. E., and H. V. Christensen, 2016, Texas through time: Lone Star geology, landscapes, and resources: Bureau of Economic Geology Udden Series no. 6, 1–431.
- Feldman, M. L., and J. R. Chairman, 1962, Southwest-northeast cross section, Marathon region to Midland Basin: West Texas Geological Society Publication.
- Frenzel, H. N., R. R. Bloomer, R. B. Cline, J. M. Cys, J. E. Galley, W. R. Gibson, J. M. Hills, W. E. King, W. R. Seager, F. E. Kottowski, and S. Thompson III, 1988, The Permian Basin region: Sedimentary cover — North American craton: US, Boulder, Colorado, Geological Society of America, *The Geology of North America*, **2**, 261–306.
- Gaherty, J. B., 2004, A surface wave analysis of seismic anisotropy beneath eastern North America: *Geophysical Journal International*, **158**, 1053–1066, doi: [10.1111/j.1365-246X.2004.02371.x](https://doi.org/10.1111/j.1365-246X.2004.02371.x).
- Galley, J. E., 1958, Oil and geology in the Permian Basin of Texas and New Mexico: North America: Habit of oil — A symposium: AAPG, Special Publication, **A215**, 395–446.
- Galley, J. E., 1970, Some principles of tectonics in the Permian Basin, *in* W. J. Stewart, ed., *Basins of the Southwest*: West Texas Geological Society Publication, **1**, 5–20.
- Gao, Z., N. D. Perez, B. Miller, and M. C. Pope, 2019, Competing sediment sources during Paleozoic closure of the Marathon-Ouachita remnant ocean basin: *Geological Society of America Bulletin*, **132**, 3–16, doi: [10.1130/B35201.1](https://doi.org/10.1130/B35201.1).
- Garcia, E. S., D. T. Sandwell, and W. H. Smith, 2014, Retracking CryoSat-2, Envisat and Jason-1 radar altimetry waveforms for improved gravity field recovery: *Geophysical Journal International*, **196**, 1402–1422, doi: [10.1093/gji/ggt469](https://doi.org/10.1093/gji/ggt469).
- Gemmer, L., S. B. Nielsen, M. Huuse, and H. Lykke-Andersen, 2002, Post-mid-Cretaceous eastern North Sea evolution inferred from 3D thermo-mechanical modeling: *Tectonophysics*, **350**, 315–342, doi: [10.1016/S0040-1951\(02\)00147-6](https://doi.org/10.1016/S0040-1951(02)00147-6).
- Graham, S. A., W. R. Dickinson, and R. V. Ingersoll, 1975, Himalayan-Bengal model for flysch dispersal in the Appalachian-Ouachita system: *Geological Society of America Bulletin*, **86**, 273–286, doi: [10.1130/0016-7606\(1975\)86<273:HMFFDI>2.0.CO;2](https://doi.org/10.1130/0016-7606(1975)86<273:HMFFDI>2.0.CO;2).
- Hall, S. A., D. E. Bird, D. J. McLean, P. J. Towle, J. V. Grant, and H. A. Danque, 2018, New constraints on the age of the opening of the South Atlantic basin: *Marine and Petroleum Geology*, **95**, 50–66, doi: [10.1016/j.marpetgeo.2018.03.010](https://doi.org/10.1016/j.marpetgeo.2018.03.010).
- Hickman, R., R. Varga, and R. Altany, 2009, Structural style of the Marathon thrust belt, West Texas: *Journal of Structural Geology*, **31**, 900–909, doi: [10.1016/j.jsg.2008.02.016](https://doi.org/10.1016/j.jsg.2008.02.016).
- Hills, J. M., 1972, Late Paleozoic sedimentation in west Texas Permian basin: *AAPG Bulletin*, **56**, 2303–2322, doi: [10.1306/819A421C-16C5-11D7-8645000102C1865D](https://doi.org/10.1306/819A421C-16C5-11D7-8645000102C1865D).
- Horak, R. L., 1985, Tectonic and hydrocarbon maturation history in the Permian Basin: *Oil & Gas Journal*, **83**, 124–129.
- Jackson, W. H., and L. C. Pakiser, 1966, Seismic study of crustal structure in the southern Rocky Mountains: US Geological survey, TL-42.
- Jarvie, D. M., D. A. Prose, B. M. Jarvie, R. J. Drozd, and A. Maende, 2017, Conventional and unconventional petroleum systems of the Delaware Basin, USA: AAPG Annual Convention and Exhibition, <http://www.searchanddiscovery.com/abstracts/html/2017/90291ace/abstracts/2612939.html>, accessed 1 February 2020.
- Keller, G. R., 2019, Constraints on structural and tectonic interpretations of the Permian Basin based on gravity and magnetic data, *in* S. C. Ruppel, ed., *Anatomy of the Paleozoic basin: The Permian Basin, USA* (vol.1, ch. 2): The University of Texas at Austin, Bureau of Economic Geology Report of Investigations 285: AAPG Memoir, **118**, 31–42.
- Kluth, C. F., P. J. Coney, M. E. Smith, and N. Riggs, 1981, Plate tectonics of the ancestral Rocky Mountains: *Geology*, **9**, no. 1, 10–15.
- Leary, R. J., P. Umhoefer, M. E. Smith, and N. Riggs, 2017, A three-sided orogen: A new tectonic model for Ancestral Rocky Mountain uplift and basin development: *Geology*, **45**, no. 8, 735–738.
- Liu, L., and D. F. Stockli, 2020, U-Pb ages of detrital zircons in lower Permian sandstone and siltstone of the Permian Basin, west Texas, USA: Evidence of dominant Gondwanan and peri-Gondwanan sediment input to Laurentia: *GSA Bulletin*, **132**, 245–262, doi: [10.1130/B35119.1](https://doi.org/10.1130/B35119.1).
- Loucks, R. G., 2008, Review of the lower Ordovician Ellenburger group of the Permian Basin, West Texas, http://www.beg.utexas.edu/resprog/permianbasin/PBGSP_members/writ_synth/EllenburgerDraft_022206.pdf, accessed on May 15 May 2020.
- Manos, T. A., and N. Perez, 2018, Thermal maturity modeling of organic-rich mudrocks in the Delaware Basin

- using Raman spectroscopy of carbonaceous material: AAPG ACE 2018.
- Marshak, S., S. Domrois, C. Abert, T. Larson, G. Pavlis, M. Hamburger, X. Yang, G. Hersch, and C. Chen, 2017, The basement revealed: Tectonic insight from a digital elevation model of the Great Unconformity, USA cratonic platform: *Geology*, **45**, 391–394, doi: [10.1130/G38875.1](https://doi.org/10.1130/G38875.1).
- Marshak, S., K. Karlstrom, and J. M. Timmons, 2000, Inversion of Proterozoic extensional faults: An explanation for the pattern of Laramide and Ancestral Rockies intracratonic deformation, United States: *Geology*, **28**, 735–738, doi: [10.1130/0091-7613\(2000\)28<735:IOPEFA>2.0.CO;2](https://doi.org/10.1130/0091-7613(2000)28<735:IOPEFA>2.0.CO;2).
- Matchus, E. J., and T. S. Jones, 1984, East-west cross section through Permian Basin of West Texas: West Texas Geological Society Publication.
- Mitchell, B. J., and M. Landisman, 1971, Geophysical measurements in the southern Great Plains, *in* G. J. Heacock, ed., The structure and physical properties of the Earth's crust: AGU, **14**, 77–93.
- Mosher, S., 1998, Tectonic evolution of the southern Laurentian Grenville orogenic belt: *Geological Society of America Bulletin*, **110**, no. 11, 1357–1375.
- Parker, R. L., 1973, The rapid calculation of potential anomalies: *Geophysical Journal International*, **31**, no. 4, 447–455.
- Pavlis, N. K., S. A. Holmes, S. C. Kenyon, and J. K. Factor, 2012, The development and evaluation of the Earth Gravitational Model 2008 (EGM2008): *Journal of Geophysical Research, Solid Earth*, **117**, 1–38, doi: [10.1029/2011JB008916](https://doi.org/10.1029/2011JB008916).
- Pawlewicz, M., C. E. Barker, and S. McDonald, 2005, Vitrinite reflectance data for the Permian Basin, West Texas and Southeast New Mexico, USGS Open-File Report, 2005-1171, accessed 1 September 2019.
- Poole, F., W. Perry, R. Madrid, and R. Amaya-Martinez, 2005, Tectonic synthesis of the Ouachita-Marathon-Sonora orogenic margin of southern Laurentia: Stratigraphic and structural implications for timing of deformational events and plate-tectonic model, *in* T. Anderson, J. Nourse, J. McKee, and M. Steiner, eds., The Mojave-Sonora megashear hypothesis: Development, assessment and alternatives: GSA Special Paper, **393**, 5453–5596.
- Romney, C., B. G. Brooks, R. H. Mansfield, D. S. Carder, J. N. Jordan, and D. W. Gordon, 1962, Travel times and amplitudes of principal body phases recorded from Gnome: *Bulletin of the Seismological Society of America*, **52**, 1057–1074.
- Ruppel, S. C., R. Loucks, C. Kerans, R. H. Jones, H. S. Nance, C. L. Breton, S. Hamlin, J. Gale, J. Kane, A. McDonnell, E. Guevara, F. Wang, R. Reed, W. Wright, H. Rowe, N. Guven, R. Day-Stirrat, D. Jarvie, H. Zeng, and Q. Fu, 2008, Integrated synthesis of the Permian Basin: Data and models for recovering existing and undiscovered oil resources from the largest oil-bearing basin in the U.S., GIS dataset, <http://www.beg.utexas.edu/research/areas/permian-basin-synthesis>, accessed 19 October 2018.
- Ruppel, S. C., ed., 2019, Anatomy of the Paleozoic basin: The Permian Basin, USA (vol.1): The University of Texas at Austin, Bureau of Economic Geology Report of Investigations 285, AAPG Memoir, **118**, 1–412.
- Shen, W., M. H. Ritzwoller, and V. Schulte-Pelkum, 2013, A 3-D model of the crust and uppermost mantle beneath the Central and Western US by joint inversion of receiver functions and surface wave dispersion. *Journal of Geophysical Research, Solid Earth*, **118**, 262–276, doi: [10.1029/2012JB009602](https://doi.org/10.1029/2012JB009602).
- Shumaker, R. C., 1992, Paleozoic structure of the Central Basin uplift and adjacent Delaware basin, west Texas: AAPG Bulletin, **76**, 1804–1824, doi: [10.1306/BDF8AD8-1718-11D7-8645000102C1865D](https://doi.org/10.1306/BDF8AD8-1718-11D7-8645000102C1865D).
- Snee, J. E. L., and M. D. Zoback, 2018, State of stress in the Permian Basin, Texas and New Mexico: Implications for induced seismicity: The Leading Edge, **37**, 127–134, doi: [10.1190/tle37020127.1](https://doi.org/10.1190/tle37020127.1).
- Soreghan, G. S., and M. J. Soreghan, 2013, Tracing Clastic delivery to the permian delaware basin, USA: Implications for paleogeography and circulation in Westernmost Equatorial Pangea tracing clastic dispersal to the Westernmost Pangean Suture: *Journal of Sedimentary Research*, **83**, 786–802, doi: [10.2110/jsr.2013.63](https://doi.org/10.2110/jsr.2013.63).
- Soto-Kerans, G. M., D. F. Stockli, X. Janson, T. F. Lawton, and J. A. Covault, 2020, Orogen proximal sedimentation in the Permian foreland basin: *Geosphere*, **16**, 567–593, doi: [10.1130/GES02108.1](https://doi.org/10.1130/GES02108.1).
- Strecker, M. R., G. E. Hillel, B. Bookhagen, and E. R. Sobel, 2011, Structural, geomorphic, and depositional characteristics of contiguous and broken foreland basins: examples from the eastern flanks of the central Andes in Bolivia and NW Argentina: *Tectonics of sedimentary basins: Recent advances*, 508–521.
- U.S. Energy Information Administration report, 2018, Permian Basin Wolfcamp Shale Play Geology review, https://www.eia.gov/maps/pdf/PermianBasin_Wolfcamp_EIARreport_Oct2018.pdf, accessed 23 February 2019.
- Van Staal, C., and A. Zagorevski, 2020, Accretion, soft and hard collision: Similarities, differences, and an application from the Newfoundland Appalachian orogen: *Geoscience Canada*, **47**, 103–118, doi: [10.12789/geocanj.2020.47.161](https://doi.org/10.12789/geocanj.2020.47.161).
- Walper, J. L., 1977, Paleozoic tectonics of the southern margin of North America: Gulf Coast Association of Geological Societies, **27**, 230–241.
- Xie, X., J. M. Anthony, and A. B. Busbey, 2019, Provenance of Permian Delaware Mountain Group, central and southern Delaware Basin, and implications of sediment dispersal pathway near the southwestern terminus of Pangea: *International Geology Review*, **61**, 361–380, doi: [10.1080/00206814.2018.1425925](https://doi.org/10.1080/00206814.2018.1425925).
- Yang, K. M., and S. L. Dorobek, 1995, The Permian Basin of west Texas and New Mexico: Flexural modeling and evidence for lithospheric heterogeneity across the Marathon Foreland: SEPM Special Publication, **52**, 37–50.



Hualing Zhang received a B.S. (2015) in geology from the University of Tulsa and the China University of Petroleum (Beijing) and an M.S. (2017) from the University of Texas at Austin. She is currently pursuing a Ph.D. in geology, and she is a graduate research assistant with the CBTH industry consortium in the Department of Earth and

Atmospheric Science at the University of Houston. Her research interests include gravity modeling and structural analysis in the Permian Basin (West Texas) and offshore Brazil.



Paul Mann received a B.A. in geology from Oberlin College and a Ph.D. from the State University of New York at Albany. His main interests include the tectonics of sedimentary basins. He is currently the Robert E. Sheriff endowed professor of geology in the Department of Earth and Atmospheric Sciences at the University of Houston,

where he also directs the CBTH Project.

Dale Bird received a Ph.D. in geophysics from the University of Houston, where he now serves as an associate research professor. He is an earth science consultant (dba Bird Geophysical) specializing in tectonophysics and the interpretation of gravity and magnetic data. He is a member of several professional societies including AAPG, AGU, EAGE, GSA, GSH, HGS, and SEG. He is the current SEG chair of the AGU-SEG joint-collaboration committee.

Kurt Rudolph worked as a petroleum geologist from 1978 to 2015, in the last 13 years serving as the chief geoscientist for ExxonMobil. He has won best paper awards for the *AAPG Bulletin* (1992 and 2017) and the *Mountain Geologist* (2015). He was an AAPG-SEG distinguished lecturer in 2001–2002 (DHI/amplitude variation with offset analysis). Currently he is an adjunct professor at Rice University and the University of Houston. His interests include tectonostratigraphy, seismic interpretation, and uncertainty analysis.